Article

Cell Host & Microbe

A conserved adaptor orchestrates co-secretion of synergistic type VI effectors in gut Bacteroidota

Graphical abstract

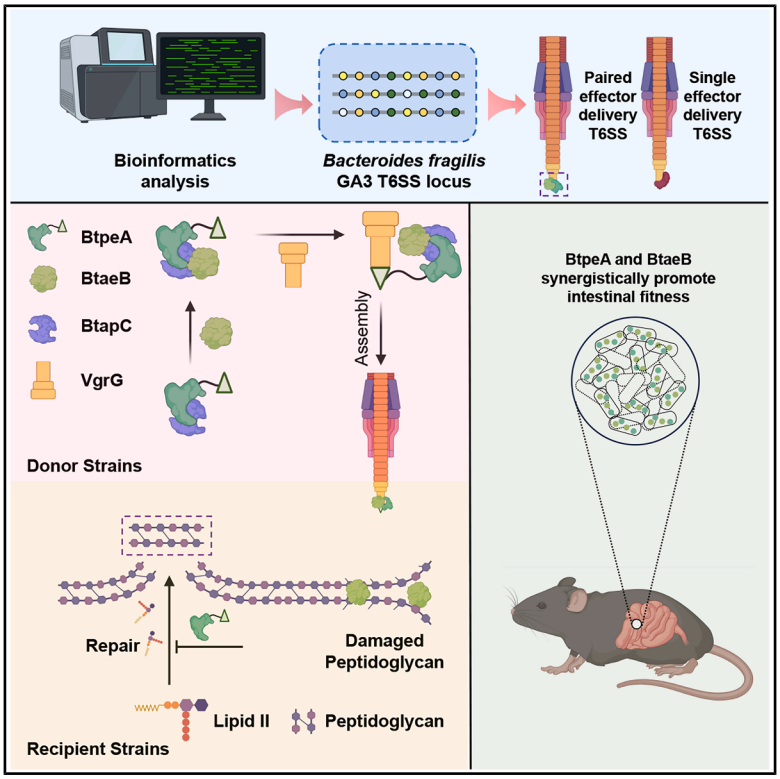

Authors

Weixun Li (李伟勋), Shuaining Zheng (郑帅宁), Xiaoning Xu (徐晓宁), ..., Bentley Lim, Feng Shao (邵峰), Xiang Gao (高翔)

Correspondence

xgao@email.sdu.edu.cn

In brief

Type VI secretion systems (T6SSs) mediate bacterial competition. Li et al. reveal that Bacteroidota T6SS effectors BtpeA and BtaeB induce distinct cell-wall destructive activities yet are co-delivered via coordinated binding to the adaptor BtapC. This conserved synergistic system enhances gut fitness of encoding strains in mice.

Highlights

- T6SS effectors BtpeA and BtaeB are distinct cell-wall-destructive enzymes
- Structural analysis elucidates the assembly mechanism of the T6SS multi-cargo complex
- Adaptor BtapC and "checkpoint" mechanism ensure co-secretion of BtpeA and BtaeB
- BtpeA and BtaeB synergistically promote gut fitness of encoding strains

Li et al., 2025, Cell Host & Microbe *33*, 1901–1915
November 12, 2025
https://doi.org/10.1016/j.chom.2025.09.012

CellPress

Cell Host & Microbe

CellPress

Article

A conserved adaptor orchestrates co-secretion of synergistic type VI effectors in gut Bacteroidota

Weixun Li (李伟勋),[1,5] Shuaining Zheng (郑帅宁),[1,5] Xiaoning Xu (徐晓宁),[1] Jing He (何静),[1] Xuyao Jiao (焦绪瑶),[1] Mingyu Wang (王明钰),[1] Wei Hu (胡玮),[1] Shengying Li (李盛英),[1] Xianzhi Jiang (蒋先芝),[2] Bentley Lim,[3] Feng Shao (邵峰),[4] and Xiang Gao (高翔)[1,6,*]

[1]State Key Laboratory of Microbial Technology, Shandong University, Qingdao 266237, China
[2]Microbiome Research Center, Moon (Guangzhou) Biotech Co. Ltd., Guangzhou 510535, China
[3]Department of Microbial Pathogenesis and Microbial Sciences Institute, Yale University School of Medicine, New Haven, CT 06536, USA
[4]National Institute of Biological Sciences (NIBS), Beijing 102206, China
[5]These authors contributed equally
[6]Lead contact
*Correspondence: xgao@email.sdu.edu.cn
https://doi.org/10.1016/j.chom.2025.09.012

SUMMARY

Interbacterial competition is crucial for shaping microbial communities and is often mediated by type VI secretion systems (T6SSs) that inject effectors into competing bacteria. T6SS effectors are released via structural proteins such as VgrG, but the secretion timing and coordination are unclear. Here, we report two effectors, BtpeA (*Bacteroides* T6SS phosphatase effector A) and BtaeB (*Bacteroides* T6SS amidase effector B), within the Bacteroidota T6SS that exert distinct cell-wall destructive activities critical for interspecies competition but whose secretion is interdependent. BtpeA and BtaeB co-secretion requires an adaptor protein, BtapC (*Bacteroides* T6SS adaptor protein C), that mediates the sequential assembly of the pre-firing complex, VgrG-BtpeA-BtaeB-BtapC. Structural analyses of this quaternary complex elucidate multi-cargo loading mechanisms with a conserved loop in BtaeB serving as a "checkpoint" to ensure BtpeA co-secretion. During mouse colonization, the combined activities of BtpeA and BtaeB significantly exceed the sum of the individual effectors. These findings unveil a T6SS-mediated co-delivery mechanism that ensures functional synergism of effectors, highlighting potential applications in modulating gut microbiota.

INTRODUCTION

Within microbial communities, organisms are densely packed, with their abundance and presence existing in a dynamic state. To establish and protect their ecological niche, bacteria secrete diverse toxins to compete with surrounding microorganisms[1–3]—these include the antimicrobial proteins secreted by the type VI secretion system (T6SS).[4] T6SSs are widely distributed among Gram-negative bacteria and primarily facilitate the contact-dependent translocation of effectors into recipient cells, disrupting their growth through diverse activities: the degradation of cell walls,[5,6] disruption of cell membrane integrity,[7,8] and digestion or modification of crucial molecules.[9–11]

Like the diverse activities exhibited by T6SS effectors, the delivery modes of these effectors also demonstrate significant variations. A subset of low molecular-weight effectors bind to Hcp (hemolysin-coregulated proteins),[12,13] while high molecular-weight effectors (>40 kDa) are loaded onto VgrG (valine-glycine repeat protein G)[14] or PAAR (proline-alanine-alanine-arginine repeat protein)[15,16] with or without adaptors for delivery.[17,18] Specialized VgrG,[19] PAAR,[20] or Hcp[21,22] proteins possess additional effector domains that serve as both structural components and functional effectors within the T6SS machinery. While the mechanisms of effector delivery have been extensively investigated using molecular genetics and biochemical assays,[16,23] detailed structural insights linking T6SS firing to the loading of multiple cargos/effectors remain largely elusive.[24]

Bacteria harboring at least one T6SS also encode multiple T6SS effectors within their genome, allowing the bacteria to effectively combat diverse competitors in various environmental conditions or minimize the emergence of resistance.[25] In some instances, the multiple effectors encoded in an individual genome and secreted by the same T6SS enhance interbacterial competition by exerting synergistic toxicity on recipients that surpass the sum of their activities.[25–28] However, whether and how the T6SS can coordinate the delivery of multiple effectors to achieve a functional synergism required for competitive success has not been reported.

T6SS has been extensively studied in Proteobacteria, where it was first identified. Recently, its presence was detected in

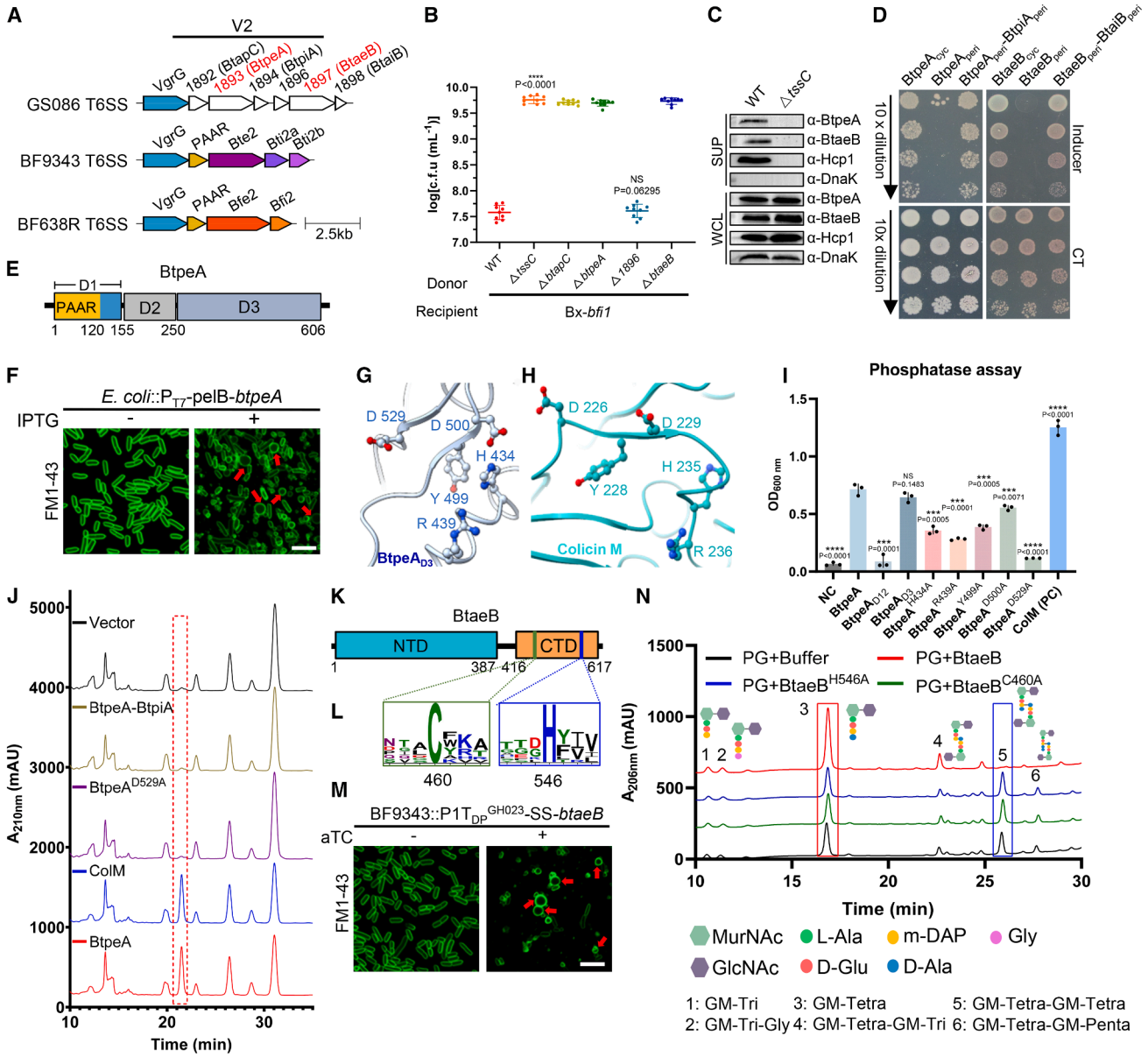

Figure 1. Two adjacent cell-wall-destructive T6SS effectors are critical for interspecies competition

(A) Schematic representation of partial T6SS loci of *B. fragilis* GS086, NCTC9343, and 638R. The two potential effectors are highlighted in red. Scale bar, 2.5 kb of T6SS loci.

(B) Co-culture assays between indicated donors and recipients. *B. xylanisolvens*::P_{TonB3}-*bfi1* serve as recipients. Colony-forming units (CFUs) of recipients were measured by selective BHI plate counts (supplemented with gentamicin and chloramphenicol). Data are presented as the mean ± SD from three independent experiments. Exact *p* values are indicated in the figure.

(C) T6SS-mediated secretion of BtpeA, BtaeB, and Hcp detected by western immunoblots in WT *B. fragilis* GS086 and its isogenic deletion mutants. WCL, whole-cell lysate; SUP, culture supernatant; DnaK, cytoplasmic loading control.

(D) Growth inhibition of *E. coli* BL21 (left) and *B. fragilis* NCTC9343 (right) carrying indicated inducible periplasmic (peri) or cytoplasmic (cyc) expression plasmids observed by 10-fold gradient dilution on agar plates with or without (CT, control group) inducer.

(E) Schematic representation of predicted functional domains in BtpeA.

(F) Confocal microscopy images of *E. coli* BL21 carrying a plasmid inducing the peri expression of BtpeA labeled with the membrane dye FM 1–43 and incubated with (+) or without (−) 0.2 mM isopropyl β-D-1-thiogalactopyranoside (IPTG) for 4 h. Red arrows point to swollen cells. Scale bar, 5 μm.

(G) Putative active sites of $BtpeA_{D3}$ are highlighted in ball sticks.

(H) Active sites of ColM (PDB: 3DA4) are shown in ball sticks.

(I) *In vitro* phosphatase activity assessed using a colorimetric assay. The lysis buffer serves as a negative control (NC), and ColM serves as a positive control (PC). Data are presented as the mean ± SD from three independent experiments. Exact *p* values are indicated in the figure.

(legend continued on next page)

Bacteroidota,[29,30] the second largest phylum found within the human gut microbiota, facilitating niche competition.[31–34] Identifying and characterizing the delivery mechanisms and mode of action of effectors from Bacteroidota T6SS have remained challenging due to the lack of predicted domains, motifs, and similarity to other proteins studied so far.[30,34–36] Therefore, it opens a new window to comprehend the multifaceted mechanisms underlying long-term investigated T6SS.

Here, we identify two effectors within *B. fragilis* T6SS V2 locus, BtpeA (*Bacteroides* T6SS phosphatase effector A) (colicin M [ColM]-like phosphatase targeting lipid II, GS086_1893) and BtaeB (*Bacteroides* T6SS amidase effector B) (peptidoglycan amidase, GS086_1897). T6SS-mediated secretion of both effectors is mutually dependent and requires adaptor BtapC (*Bacteroides* T6SS adaptor protein C), encoded within the same locus (Figures 1A and S1A). BtapC-BtpeA binding initiates the assembly of the BtpeA-BtaeB-BtapC ternary complex, which is essential for loading both effectors onto VgrG. The cryoelectron microscopy (cryo-EM) structure of the BtpeA-BtaeB-BtapC-VgrG quaternary complex and subsequent biochemical analysis elucidate precise multi-cargo loading mechanisms. Additionally, a highly conserved loop region within BtaeB provides a distinct "checkpoint" mechanism to ensure co-secretion of both effectors. Comparative genomic analysis reveals that >50% of total *B. fragilis* GA3 (genetic architecture 3) T6SS employ the BtapC-orchestrated delivery system, establishing BtapC-mediated cargo assembly as a hallmark of multi-effector co-secretion in this prevalent T6SS subtype. Animal models and bioinformatic analysis demonstrated that BtapC-mediated effector co-secretion confers intestinal fitness to encoding strains via synergistic functionality, a mechanism conserved among gut Bacteroidota, highlighting the potential for engineering diverse T6SS effector pairs to modulate gut microbiome dynamics.

RESULTS

A *B. fragilis* T6SS V2 locus bearing two effectors critical for interspecies competition

The GA3 T6SS is widely distributed across *B. fragilis* species,[30,37,38] featuring two variable regions (V1 and V2) that exhibit a higher degree of genetic diversity.[30] Unlike the T6SS V2 region of *B. fragilis* strains NCTC9343 and 638R,[31,32] the recently isolated *B. fragilis* strain GS086 exhibits a unique genetic architecture in its T6SS V2 region, featuring six genes with unknown functions (Figures 1A and S1A). Bioinformatic analysis[39] revealed that both BtpiA (GS086_1894, *Bacteroides* T6SS phosphatase immunity protein A) and BtaiB (GS086_1898, *Bacteroides* T6SS amidase immunity protein B) carry a putative Sec signal peptide (SP) sequence, while the proteins encoded by their adjacent genes, BtpeA and BtaeB, lack the SP. This implies that BtpeA-BtpiA and BtaeB-BtaiB are likely T6SS effector-immunity pairs. Therefore, we generated a set of GS086 isogenic mutants, including individual deletions of each putative effector (Δ*btpeA* and Δ*btaeB*) and two function-unknown genes (Δ*btapC* and Δ*GS086_1896*) to investigate whether these genes conferred a T6SS-mediated competitive advantage during interspecies competition *in vitro*.

When a susceptible *B. xylanisolvens* was employed as the recipient strain to assess contact-dependent antagonism by these proteins, it was observed that the mutants lacking putative effectors Δ*btpeA* and Δ*btaeB*, as well as Δ*btapC* but not Δ*GS086_1896*, exhibited a complete loss of antagonism, similar to the T6SS-inactivated strain (GS086Δ*tssC*) (Figure 1B). Secretion assays and growth inhibition assays further confirmed that BtpeA and BtaeB are T6SS-secreted effectors functioning in the periplasm of susceptible host strains (Figures 1C and 1D). Co-expression of putative cognate immunity protein BtpiA or BtaiB in the periplasm of susceptible host strains effectively mitigated the toxicity of the effector in susceptible host strains, respectively (Figure 1D). These findings collectively indicate that BtpeA and BtaeB are critical T6SS effectors involved in interspecies competition.

BtpeA and BtaeB are potent but distinct cell-wall-destructive enzymes

To gain insight into the cellular activity of both effectors, we queried their functional domains using JackHMMER,[40] which revealed a PAAR domain and two uncharacterized domains in BtpeA (Figure 1E). A comprehensive analysis of the whole genome annotation of GS086, together with InterproScan[41] results, indicated that BtpeA is the sole protein containing the PAAR motif. We then performed fluorescence microscopy to observe morphological changes in *Escherichia coli* upon expressing periplasmic BtpeA, which resulted in cellular swelling and lysis, indicating a potential compromise of cell-wall integrity by BtpeA (Figure 1F). Agar spot assays further demonstrated that domain 3 (D3) of BtpeA exhibited the comparable inhibitory effect as the full-length protein when expressed in *E. coli* (Figure S1B). To identify the mechanism underlying BtpeA-induced toxicity, we determined the crystal structure of the toxic domain $BtpeA_{D3}$ in complex with BtpiA at 2.11 Å resolution (Figure S1C; Table S1). Structural homology searches by DALI[42] reveal a notable structural similarity between $BtpeA_{D3}$ and the enzymatic domain of ColM (PDB: 3DA4) (Figures 1G, 1H, and S1D). ColM is a phosphatase that degrades lipid II,[43–45] an essential building block for peptidoglycan construction

(J) Partial HPLC chromatograms of *E. coli* BL21 membrane lipid extract resulting from the peri expression of the indicated protein. Vector serves as a NC. The red dashed boxes indicate significant changes in peaks observed after the peri expression of ColM and BtpeA compared with the NC group.
(K) Schematic representation of predicted functional domains in BtaeB. NTD, N-terminal domain; CTD, C-terminal domain.
(L) Sequence logos generated from alignments of BtaeB and selected C39 family peptidases. Conserved active sites corresponding to BtaeB are shown below the sequence logos.
(M) Confocal microscopy images of *B. fragilis* NCTC9343 carrying a plasmid inducing the peri expression of BtaeB labeled with the membrane dye FM 1–43 and incubated with (+) or without (−) 100 ng/mL anhydrotetracycline (aTC) for 4 h. Red arrows point to swollen cells. Scale bar, 5 μm.
(N) Partial HPLC chromatograms of sodium borohydride-reduced soluble *E. coli* peptidoglycan fragments resulting from the digestion of BtaeB or BtaeB mutants. Red and blue boxes indicate NAG-NAM-tetrapeptides (N-acetylglucosamine-N-acetylmuramic acid tetrapeptides, GM-tetrapeptide) and GM-tetrapeptide-GM-tetrapeptide, respectively.
For (B)–(D), (F), (I), (J), (M), and (N), experiments were conducted at least three times with consistent results.

in bacteria.[46] The structural analysis comparing $BtpeA_{D3}$ with ColM identified residues His434, Arg439, Tyr499, Asp500, and Asp529 as putative active sites of BtpeA (Figures 1G and 1H).

Consistent with ColM, both BtpeA and $BtpeA_{D3}$ exhibited phosphatase activity *in vitro*. Targeted mutations of putative active sites in BtpeA exhibited a decrease in phosphatase activity (Figure 1I). Agar spot assays and fluorescence microscopy of respective mutants nearly abolished the antibacterial toxicity of BtpeA in susceptible cells (Figures S1E and S1F). Subsequent high-performance liquid chromatography (HPLC) analysis was performed on membrane lipid extracts obtained from periplasmic expression of BtpeA, its isogenic variants, and ColM in *E. coli*. The peak profiles of membrane lipid extracts resulting from the expression of BtpeA, but not its isogenic variant, exhibited a comparable pattern to those observed upon expressing ColM (Figure 1J). Our findings demonstrate that BtpeA is a ColM-like phosphatase that targets lipid II.

Meanwhile, BtaeB was identified to comprise an N-terminal domain (NTD) of unknown function and a C-terminal domain (CTD) belonging to the characterized C39 family peptidase, sharing conserved active site residues at Cys460 and His546[47] (Figures 1K and 1L). Morphological changes in cell swelling and lysis were also observed upon expressing periplasmic BtaeB in *B. fragilis* NCTC9343 by fluorescence microscopy, implying the potential targeting of the peptidoglycan cell wall by BtaeB (Figure 1M). To test this hypothesis, we incubated purified BtaeB with purified peptidoglycan sacculi and analyzed the reaction product using HPLC.[48] Similar to the T6SS amidase effector 2 (Tae2),[5] BtaeB cleaved peptidoglycan tetrapeptide-tetrapeptide crosslinks at the D, D amide bond between meso-diaminopimelic acid (mDAP) and D-alanine (Figure 1N). Targeted mutations of the conserved active sites (Cys460 and His546) in BtaeB completely abolished its amidase activity (Figures 1N, S1G, and S1H). Our findings demonstrate that BtaeB is an amidase that targets peptidoglycan.

T6SS-mediated secretion of BtpeA and BtaeB is mutually dependent

To further validate the significance of the enzymatic activities exhibited by these two T6SS effectors during interbacterial competition *in vitro*, we generated a set of GS086 isogenic mutants in one or both effectors, enabling us to directly attribute any observed fitness differences to the specific effector under investigation. When the GS086 isogenic strain (Δ*btpA*Δ*btpiA*Δ*btaeB* Δ*btaiB*) or a susceptible *B. xylanisolvens* was used as the recipient strain to evaluate contact-dependent antagonism by two effectors, it was observed that either $BtpeA^{D529A}$ or $BtaeB^{H546A}$ significantly diminished but did not altogether abolish the antagonism. The complete loss of antagonism was achieved by the V2 inactive-effector mutant ($BtpeA^{D529A}$-$BtaeB^{H546A}$) (Figures 2A and 2B). Consistent with the above observations, complementation of susceptible recipients (Δ*btpA*Δ*btpiA*Δ*btaeB*Δ*btaiB*) with *btpiA* or *btaiB* alone partially restored resistance against wild-type (WT) GS086 in competition assays. Notably, dual complementation with both immunity proteins significantly enhanced resistance compared with individual gene expression (Figure S1I).

Surprisingly, a substantial phenotypic difference was observed between the effector point mutants and the effector deletion mutants during co-culture competitions (Figures 2A and 2B). The inactivated mutants $BtpeA^{D529A}$ and $BtaeB^{H546A}$ retained discernible antagonistic activity, while the deleted mutants Δ*btpeA* and Δ*btaeB* displayed a complete loss of antagonistic activity without any additive effects (Figures 2A and 2B). Subsequent secretion assays revealed that deletion of any effector in the V2 region resulted in complete abrogation of secretion for the remaining effector, while intracellular expression levels remained unaffected (Figures 2C and S1J). Moreover, individual deletion of either effector significantly impaired Hcp secretion (Figure 2C), a widely used indicator for assessing T6SS activity.[31] Importantly, the inactivated effector mutants did not affect the secretion of both effectors and Hcp (Figure 2C). These findings indicate that T6SS-mediated secretion of BtpeA and BtaeB is mutually dependent.

BtapC within the T6SS locus is required for the co-secretion of BtpeA and BtaeB

To elucidate the mechanism underlying the co-secretion of BtpeA and BtaeB, we initially investigated their potential to form a complex. However, no direct interactions between BtpeA and BtaeB were observed using pull-down analysis (Figure 2D). Given that BtapC, the uncharacterized protein in the V2 region of GS086 T6SS, significantly reduced the T6SS-mediated interspecies competition (Figures 1A, 1B, 2A, and 2B), we subsequently investigated its involvement in T6SS secretion. Notably, the BtapC deletion mutant (Δ*btapC*) also displayed no detectable secretion of both effectors and a reduction in Hcp secretion (Figure 2E). Consistent with the results of co-culture competitions, the GS086_1896 deletion mutant (Δ*1896*) did not exhibit any defect in T6SS secretion (Figures 1B, 2A, 2B, and 2E).

Binding of BtapC to BtpeA triggers BtpeA-BtaeB-BtapC ternary complex formation

Considering the genetic linkage of BtapC, BtpeA, and BtaeB, along with their shared secretion defect, we tested the potential that these three proteins formed a protein complex required for T6SS secretion. Notably, BtpeA was observed to form a binary complex with BtapC (Figures 2F and 2G). Although direct interactions between BtaeB and either BtpeA or BtapC were not initially detected (Figures 2D and 2F), subsequent engagement of BtaeB with the binary complex formed by BtpeA-BtapC was evident (Figures 2F and 2H). These findings indicate that BtpeA, BtaeB, and BtapC form a ternary complex, which necessitates the presence of the BtpeA-BtapC binary complex. Therefore, we designated the role of BtapC as an adaptor within the ternary complex.

Only the BtpeA-BtapC-BtaeB ternary complex can be loaded onto VgrG

The subsequent incorporation of BtaeB relied on the preformation of the binary complex BtpeA-BtapC, which could explain the observed effect of a BtpeA-deleted mutant on BtaeB secretion. However, it was surprising to observe the decreased secretion of BtpeA and Hcp in the BtaeB-deleted mutant. Previous work has shown that PAAR domains of T6SS effectors can interact with VgrG, thereby facilitating their secretion.[15,49] The absence of the PAAR repeat prevents the proper assembly and function of the

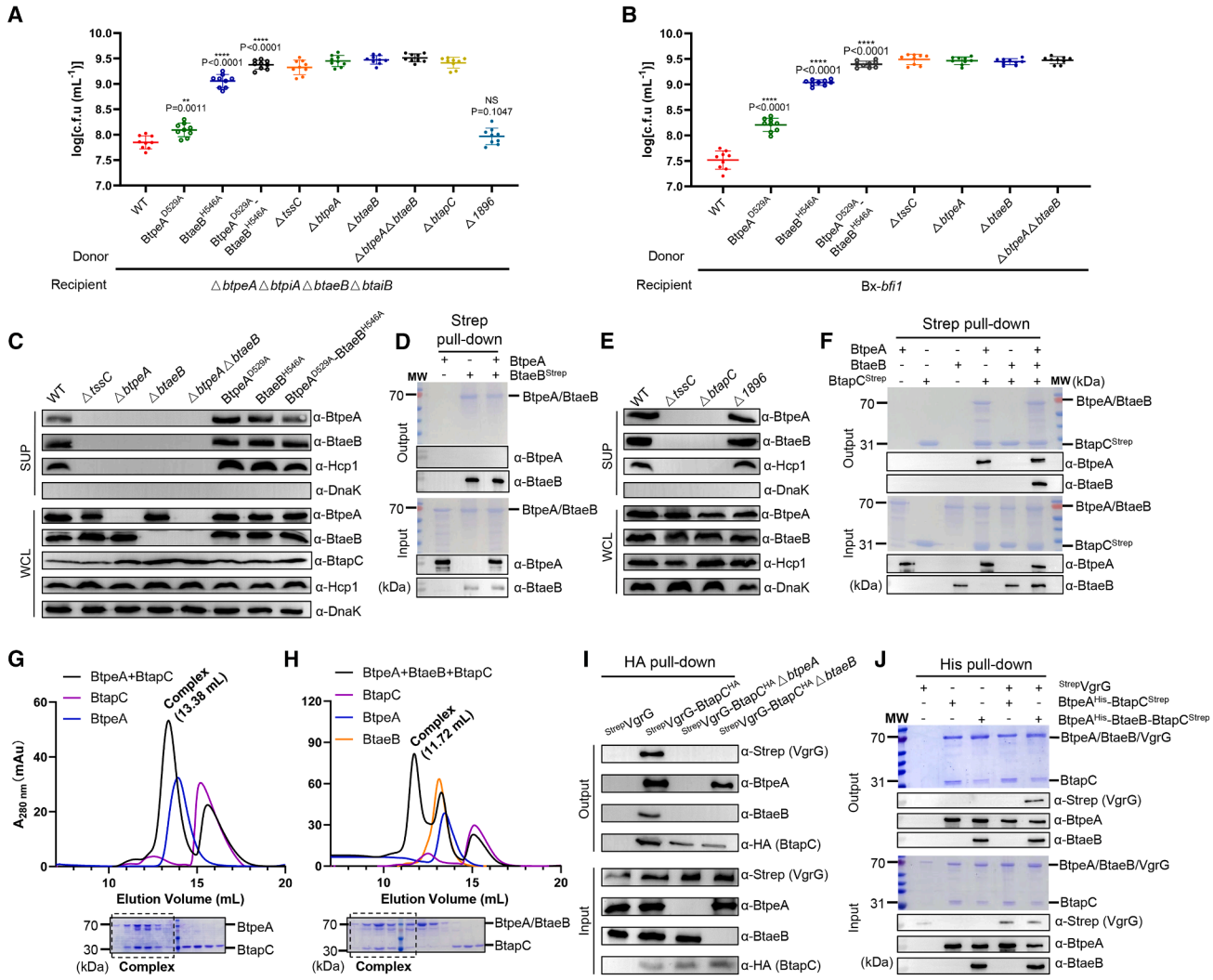

Figure 2. The formation of the ternary complex is orchestrated by BtapC and subsequently loaded onto VgrG

(A and B) Co-culture assays between indicated donors and recipients. GS086 isogenic sensitive mutant GS086Δ*btpeA*Δ*btpiA*Δ*btaeB*Δ*btaiB* (A) and *B. xylanisolvens*::P_{TonB3}-*bfi1* (B) serve as recipients, respectively. CFU of recipients were measured by selective BHI plate counts. Data are presented as the mean ± SD from three independent experiments. Exact *p* values are indicated in the figure.

(C) T6SS-mediated secretion of the indicated proteins detected by western immunoblots in WT *B. fragilis* GS086 and its isogenic deletion mutants.

(D) Pull-down analysis to detect the interaction between the purified strep-tagged BtaeB and BtpeA.

(E) T6SS-mediated secretion of the indicated proteins detected by western immunoblots in WT *B. fragilis* GS086 and its isogenic deletion mutants.

(F) Pull-down analysis to detect the interaction between the purified strep-tagged BtapC, BtpeA, and BtaeB.

(G and H) The interaction assay between the purified BtpeA and BtapC (G) or BtpeA, BtaeB, and BtapC (H) by gel filtration chromatogram and SDS-PAGE analysis.

(I) Co-immunoprecipitation (coIP) analysis to detect the interactions of VgrG, BtpeA, BtaeB, and BtapC proteins in GS086, the *btpeA* deletion strain, or the *btaeB* deletion strain. WCLs were used as input for coIP. Coprecipitated proteins (output) were detected by western immunoblots with antibodies specific to indicated proteins.

(J) Pull-down analysis to detect the interaction between the purified strep-tagged VgrG and binary complex (BtpeA-BtapC) or ternary complex (BtpeA-BtaeB-BtapC).

For (A)–(J), experiments were conducted at least three times with consistent results.

T6SS apparatus, resulting in a substantial impairment in Hcp secretion.[50] Motivated by the finding that BtpeA contains a PAAR domain (Figure 1E), we hypothesized that the BtpeA-BtaeB-BtapC ternary complex might associate with VgrG and subsequently delivered by T6SS, wherein BtaeB plays a role in facilitating the association between BtpeA and VgrG.

To validate this hypothesis, we investigated the formation of the proposed quaternary complex in GS086 and *in vitro*. Co-immunoprecipitations (coIPs) conducted in GS086 confirmed the existence of this putative quaternary complex comprising VgrG, BtpeA, BtaeB, and BtapC (Figure 2I). Additionally, *in vitro* interaction assays further corroborated the

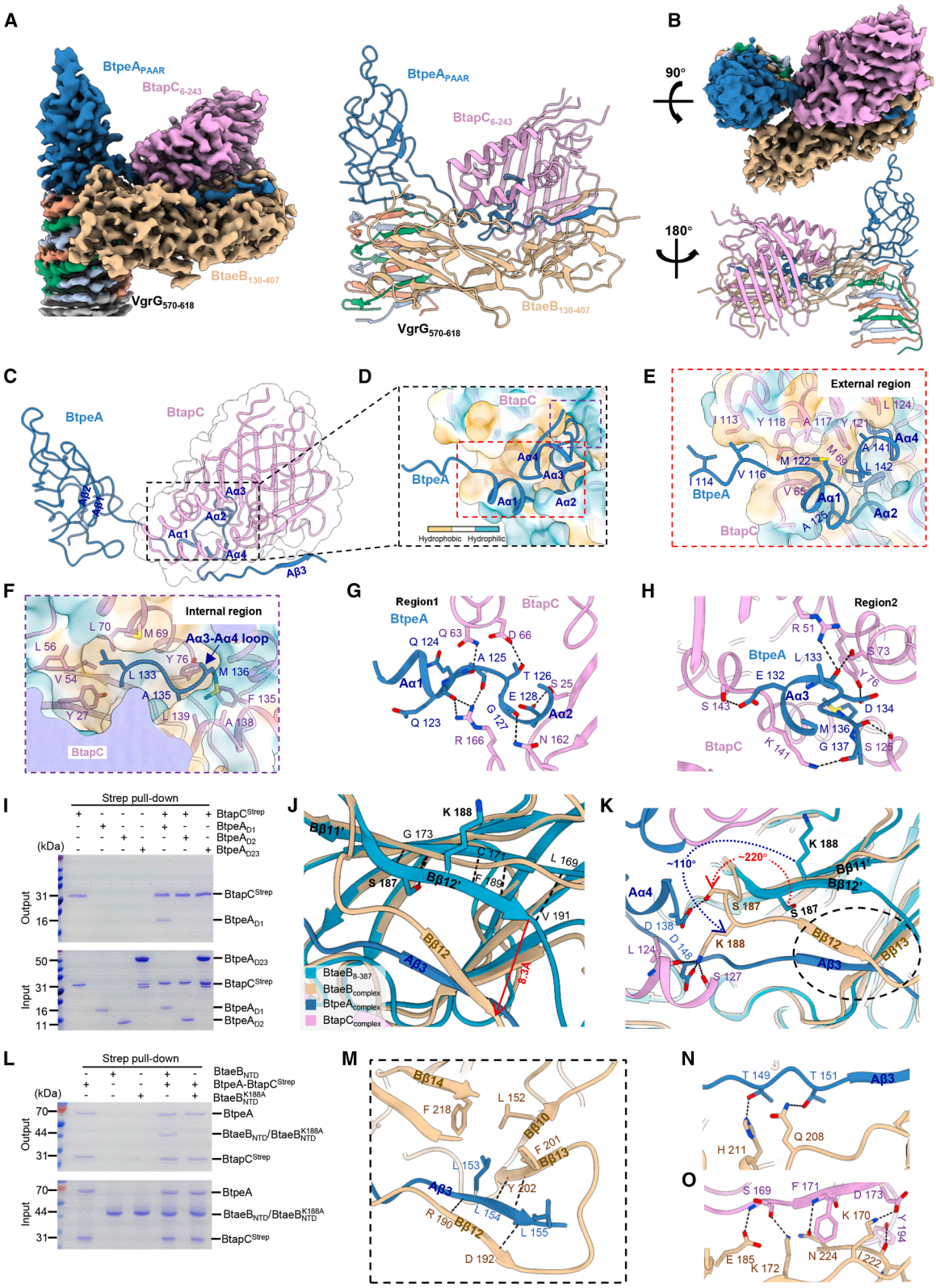

(legend on next page)

formation of this complex (Figure 2J). The coIP assay further confirmed that the BtpeA-BtapC complex is essential for interaction with BtaeB and VgrG *in vivo* (Figure 2I). However, no interaction between VgrG and BtpeA-BtapC was observed neither in the BtaeB-deleted mutant strain (Figure 2I) nor *in vitro* (Figure 2J), indicating that BtaeB plays an essential role in promoting BtpeA loading onto VgrG, thereby enabling the co-delivery of two effectors.

Cryo-EM structure and architecture of the VgrG-BtpeA-BtaeB-BtapC quaternary complex

To elucidate the mechanism of BtapC-mediated formation of the BtpeA-BtaeB-BtapC ternary complex and unravel its mechanism underlying the co-delivery of both effectors, we determined the single-particle cryo-EM structure of the $VgrG_{570–618}$-$BtpeA_{2–156}$-$BtaeB_{130–407}$-$BtapC_{6–243}$ quaternary complex at a resolution of 3.06 Å, providing unprecedented insights into the intricate arrangement of multiple cargos loaded onto the tip region of the T6SS (Figures 3A, 3B, S2A–S2D, S3A, and S3B; Table S2). Although *in vitro* pull-down analysis showed no detectable interaction between BtpeA and BtaeB, as well as BtaeB and BtapC (Figures 2D and 2F), the interaction between BtpeA and BtaeB and that of BtaeB and BtapC were resolved clearly in the quaternary complex structure (Figures 3A and 3B).

Structural mechanism for BtaeB docking onto the BtpeA-BtapC binary complex

Several adaptor proteins have been identified in the Proteobacteria T6SS, although their functional mechanisms are not yet fully understood. Structural alignment analysis revealed low similarity (root-mean-square deviation [RMSD] > 10 Å; Figure S3C) between BtapC and previously reported adaptor families such as DUF4123 (Tec/Tap),[51] DUF1795 (DcrB/Eag),[52] and DUF2169.[53] Moreover, InterPro domain scans failed to identify any recognizable domains within BtapC, further supporting its distinct nature. To elucidate the role of BtapC as a unique adaptor protein in initiating the sequential formation of the BtpeA-BtapC-BtaeB ternary complex, we initially investigated the interaction between BtpeA and BtapC. The BtapC protein adopts an open shell-like structure, with the α1-α4 of BtpeA (Aα1-Aα4) tightly gripped and elevated within the cavity formed by BtapC, while the β3 of BtpeA (Aβ3) flanked around BtapC (Figure 3C). This specific architecture of the BtpeA-BtapC binary complex may serve as the structural basis for accommodating BtaeB and facilitating the sequential assembly of the BtpeA-BtapC-BtaeB ternary complex.

Closer inspections revealed that interactions between BtpeA and BtapC are facilitated by a vast network of hydrophobic (Figures 3D–3F) and polar interactions (Figures 3G and 3H). The hydrophobic interactions are observed at both the external (Figure 3E) and internal (Figure 3F) regions of the hydrophobic pocket of BtapC, with the insertion of residues from the α1-α4 of BtpeA (Aα1-Aα4, residues Ile114-Leu142). The polar interactions can be divided into regions 1 (Figure 3G) and 2 (Figure 3H), where extensive polar interactions occur between residues from the Aα1-Aα3 and those from BtapC. Consistent with the extensive interactions between the Aα1-Aα4 and BtapC observed above, pull-down analysis further confirmed a direct interaction between $BtpeA_{D1}$ (residues Met1-Leu155) and BtapC, while no direct interaction was observed between $BtpeA_{D2}$ (residues Lys156-Ile250) or $BtpeA_{D23}$ (residues Lys156-end) and BtapC (Figure 3I, lanes 5–7). CoIP assays using GS086 BtpeA truncated mutants further confirmed that only BtpeA and $BtpeA_{D1}$ could form the quaternary complex, whereas $BtpeA_{D23}$ failed to interact with BtapC (Figure S4A). In line with the above observations, only BtpeA and $BtpeA_{D1}$ supported efficient secretion of both effectors (Figure S4B).

To further dissect the docking mechanism of BtaeB onto the BtpeA-BtapC binary complex, we determined the crystal structure of $BtaeB_{8–387}$ at 2.18 Å resolution (Figure S4C; Table S1). By superimposing the crystal structure of $BtaeB_{8–387}$ onto the VgrG-BtpeA-BtaeB-BtapC quaternary complex, we observed significant conformational changes in BtaeB upon binding to the BtpeA-BtapC binary complex (Figure 3J). The crystal structure of $BtaeB_{8–387}$ reveals an antiparallel arrangement between its β12′ and β11′ (Bβ12′ and Bβ11′), facilitated by main-chain polar interactions (Figure 3J). However, binding to the BtpeA-BtapC complex induces a remarkable conformational change in Bβ12 (∼8 Å movement), resulting in a parallel arrangement with Aβ3 (Figure 3J) and a ∼110° rotation of Lys188 in Bβ12 (Figure 3K). This directs the side chain of Lys188 to form polar interactions with Asp148 of BtpeA as well as with Leu124 and Ser127 of BtapC, which places Lys188 of BtaeB at the center of the interaction between BtaeB, BtpeA, and BtapC

Figure 3. Architecture of the VgrG-BtpeA-BtaeB-BtapC complex

(A and B) Overall structure of the $VgrG_{570–618}$-$BtpeA_{2–156}$-$BtaeB_{130–407}$-$BtapC_{6–243}$ complex depicted with cryo-EM maps presented in frontal and top views, and the ribbon model presented in frontal and posterior views. Colors indicate different proteins.

(C–H) Structure of the BtpeA in complex with BtapC (C). The surface of BtapC is colored by its hydrophobicity (hydrophilic, cyan; neutral, white; hydrophobic, golden), with BtpeA shown in ribbon (D). Hydrophobic interactions in external (E) and internal (F) regions are indicated by red and purple dashed rectangles, respectively. Polar interactions are divided into regions 1 (G) and 2 (H).

(I) Pull-down analysis to detect the interaction of strep-tagged BtapC with BtpeA or the individual domain of BtpeA.

(J) Structural comparison between the crystal structure of $BtaeB_{8–387}$ (cyan) and BtaeB (tan) in the $VgrG_{570–618}$-$BtpeA_{2–156}$-$BtaeB_{130–407}$-$BtapC_{6–243}$ complex structure revealing a conformational change in Bβ12′ (β12′ of $BtaeB_{8–387}$ crystal structure). Main-chain polar interactions between Bβ11′ and Bβ12′ are indicated by black dashed lines. The distance between Bβ12′ and Bβ12 (β12 of BtaeB in the complex) is indicated by a red arrow.

(K) Detailed conformation changes in BtaeB. Rotation of K188 and S187 are indicated by blue and red dashed arrows, respectively. Polar interactions are indicated by the black dashed lines.

(L) Pull-down analysis to detect the interaction of the $BtpeA\text{-}BtapC^{strep}$ binary complex with the NTD of BtaeB ($BtaeB^{NTD}$) or the indicated $BtaeB^{NTD}$ variant.

(M) Close-up view of the interactions between β3 of BtpeA (Aβ3) and BtaeB (the dashed elliptical region in K). Main-chain interactions are indicated by black dashed lines, while residues involved in hydrophobic interactions are displayed as sticks.

(N and O) Extensive interactions in the BtpeA-BtapC-BtaeB ternary complex. Polar interactions between BtaeB and BtpeA (N), as well as between BtaeB and BtapC (O), are indicated by black dashed lines.

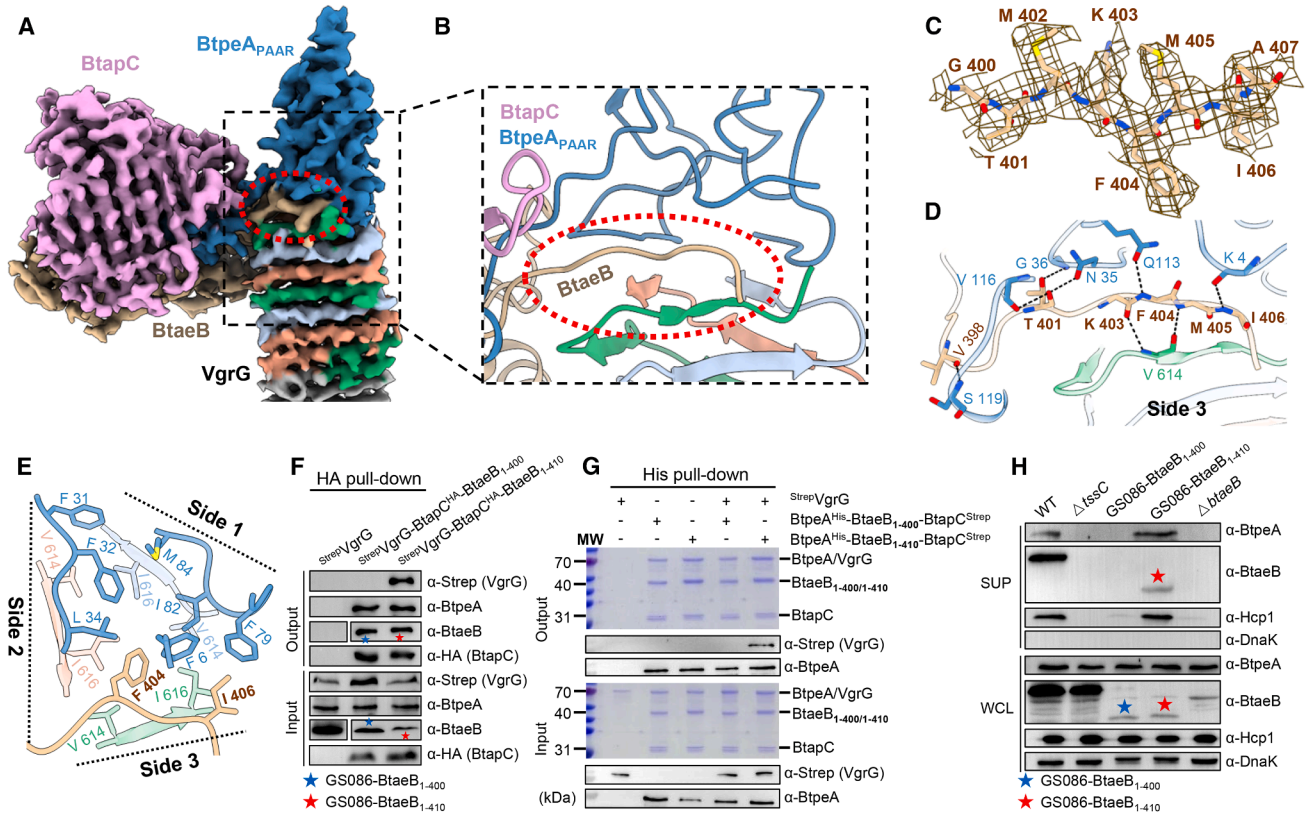

Figure 4. BtaeB-derived loop is essential for the co-secretion of BtpeA and BtaeB

(A and B) Overall structure of the VgrG$_{570–618}$-BtpeA$_{2–156}$-BtaeB$_{130–407}$-BtapC$_{6–243}$ complex depicted in the cryo-EM map from a back view (A). BtaeB$_{400–407}$ loop (highlighted in the red dashed elliptical region) inserts into the interaction interface between VgrG and the PAAR-like domain of BtpeA, shown in a ribbon model within a black dotted rectangle (B).

(C) Electron density of BtaeB$_{400–407}$ in the VgrG$_{570–618}$-BtpeA$_{2–156}$-BtaeB$_{130–407}$-BtapC$_{6–243}$ complex.

(D and E) Close-up view of the interactions at the interface of the VgrG, BtpeA, and BtaeB, highlighting both polar (D) and hydrophobic (E) interactions. Residues mediating interactions are labeled and shown as sticks; polar interactions are indicated by black dashed lines.

(F) CoIP analysis to detect the interactions of VgrG, BtpeA, BtaeB, and BtapC proteins in GS086 or BtaeB truncation strains. WCLs were used as input for coIP. Coprecipitated proteins (output) were detected by western immunoblots with antibodies specific to indicated proteins. The apparent segmentation of the BtaeB band is the result of cropping distinct molecular-weight regions from this same membrane to emphasize the relevant protein bands.

(G) Pull-down analysis to detect the interactions between the purified strep-tagged VgrG and the indicated ternary complex with (BtpeA-BtaeB$_{1–410}$-BtapC) or without the BtaeB-derived loop (BtpeA-BtaeB$_{1–400}$-BtapC).

(H) T6SS-mediated secretion of the indicated proteins detected by western immunoblots in WT *B. fragilis* GS086 and its isogenic deletion mutants.

For (F) and (H), blue asterisk: GS086-BtaeB$_{1–400}$; red asterisk: GS086-BtaeB$_{1–400}$. Experiments were conducted at least three times with consistent results.

(Figure 3K). Consistent with the interactions observed above, subsequent pull-down analysis further confirmed that the targeted mutation of Lys188 disrupted the interaction between BtaeB and the BtpeA-BtapC complex (Figure 3L, lanes 4–5). Additionally, the hydroxyl group of Ser187 in BtaeB rotated ~220°, forming a polar interaction with Asp138 of BtpeA (Figure 3K).

Further structural analysis revealed extensive interactions between BtaeB and Aβ3, including main-chain interactions between Aβ3 and Bβ12 and Bβ13; hydrophobic interactions involving Leu153 and Leu155 in Aβ3 and Leu152, Phe201, and Phe218 in BtaeB (Figure 3M); and polar interactions between Thr149 and Thr151 in Aβ3 and Gln208 and His211 in BtaeB (Figure 3N). These extensive interactions with Aβ3 further enhance the binding of BtaeB to BtapC through a network of polar interactions involving the side chain of Lys170, Lys172, Glu185, Asn224, and the main chain of Ile222 in BtaeB (Figure 3O). All these interactions collectively contribute to forming the BtpeA, BtaeB, and BtapC complex for their co-delivery.

The ternary complex presents a BtaeB-derived loop that critically binds to VgrG

During the atomic modeling of the VgrG-BtpeA-BtaeB-BtapC quaternary complex, we observed additional electron density at the interface between VgrG and BtpeA$_{PAAR}$ (Figures 4A and 4B). Furthermore, utilizing the model-angelo,[54] we determined that the unassigned electron density unambiguously corresponded to a loop of BtaeB (BtaeB$_{400–407}$) (Figures 4A–4C).

The interface between VgrG and BtpeA$_{PAAR}$ adopts a triangular conformation wherein the BtaeB$_{400–407}$ loop is inserted into one side of the triangle, facilitating polar and hydrophobic

interactions with both proteins (Figures 4D, 4E, and S4D). Residues Thr401, Lys403, Phe404, Met405, and Ile406 of BtaeB established polar interactions with VgrG and BtpeA in the side 3 region (Figure 4D). Phe404 and Ile406 also extend toward the interface of hydrophobic contacts formed by VgrG and BtpeA (Figure 4E). Additionally, VgrG and BtpeA participate in a series of side-chain hydrophobic and main-chain polar interactions in the side 1 and side 2 regions (Figures 4E and S4D).

The unique loop in BtaeB is essential for co-secretion of the two effectors

Based on the observed secretion and interaction results (Figures 2C, 2I, and 2J), we postulated that BtaeB potentially facilitated the loading and secretion of BtpeA through its loop region ($BtaeB_{400–407}$). To test this hypothesis, we initially generated GS086 isogenic mutants to examine the formation of the VgrG-BtpeA-BtaeB-BtapC quaternary complex using truncated BtaeB mutants with or without the loop.

In vivo coIP assays and *in vitro* pull-down assays both demonstrated that the BtaeB truncated mutant (GS086-$BtaeB_{1–410}$, including the loop) could assemble the VgrG-BtpeA-BtaeB-BtapC quaternary complex (Figures 4F and 4G), resulting in secretion levels of BtpeA and Hcp comparable to those of the WT strain (Figure 4H). Conversely, the absence of the unique loop in BtaeB (GS086-$BtaeB_{1–400}$, excluding the loop) led to the inability to form this quaternary complex (Figures 4F and 4G) and consequently abolished the secretion of BtpeA, BtaeB, and Hcp (Figure 4H). Notably, even without the essential loop, BtaeB could still form the BtpeA-BtaeB-BtapC ternary complex (Figures 4F and 4G). These findings highlight that the critical loop region (residues Gly400-Ala407), derived from BtaeB, plays an essential role in loading $BtpeA_{PAAR}$ onto VgrG. This process facilitates the assembly of the VgrG-BtpeA-BtaeB-BtapC quaternary complex, ensuring simultaneous delivery of both BtpeA and BtaeB to recipient strains via the T6SS.

Co-secreted BtpeA and BtaeB synergistically promote intestinal fitness of *B. fragilis*

The identified quaternary complex ensures the maturation of the T6SS machinery and facilitates the simultaneous secretion of both BtpeA and BtaeB during each injection. To gain insights into the significance underlying the co-secretion of BtpeA and BtaeB in T6SS-mediated antagonism within the mammalian gut, we monocolonized or co-colonized effector-sensitive GS086 isogenic recipient (Δ*btpeA*Δ*btpiA*Δ*btaeB*Δ*btaiB*) with the equivalent amounts of the WT GS086 or mutant donor strains in antibiotic-treated mice (Figures 5A and S5A).

During monocolonization experiments, both the WT donor and effector-sensitive GS086 isogenic recipient maintained stable colonization capacity (Figure S5B). However, during co-colonization experiments, 29 days post gavage, the recipient strain co-colonized with the V2 inactive-effector mutant ($BtpeA^{D529A}$-$BtaeB^{H546A}$, black line) or the BtaeB inactive mutant ($BtaeB^{H546A}$, blue line) showed similar abundance when compared with co-colonization with a T6SS-inactivated donor strain (Δ*tssC*, orange line) (Figure 5B), suggesting that BtpeA activity does not contribute significantly to the antagonistic activity *in vivo*. By contrast, the abundance of the sensitive strain decreased ~10^3-fold when co-colonized with the donor strain where BtpeA is inactive ($BtpeA^{D529A}$, green line) (Figure 5B). The abundance of the GS086 sensitive recipient strain co-colonized with WT GS086 (red line) decreased by ~10^5-fold compared with its abundance when co-colonized with the T6SS-inactivated donor strain (Δ*tssC*) (Figure 5B). These results suggest that BtpeA, as the sole effector, contributed minimally to antagonism toward the sensitive recipient strain in the mammalian gut. By contrast, BtaeB contributed to ~1/100 (10^3-fold, see green line /10^5-fold, see red line) of the observed antagonistic activity *in vivo* (Figure 5B). Similar phenotypes were observed in competitive colonization experiments between the sensitive recipients complemented with immunity genes and the donor WT GS086 (Figures S5C and S5D). These findings indicate that the combined activities of BtpeA and BtaeB significantly exceeded the sum of their individual effectors, implying a synergistic boost of interbacterial competition through the co-secretion of these two effectors.

BtapC-mediated effector co-secretion is conserved in human gut Bacteroidota

To assess the potential of diverse *B. fragilis* strains in employing this efficient T6SS-mediated antagonistic mechanism, we conducted an extensive search across all published *B. fragilis* genomes available in the NCBI database (1,623, updated to December 2024) using BtapC as the query sequence. Our analysis revealed that ~13.7% (223 out of 1,623) of *B. fragilis* strains encode the GS086-type T6SS V2 region that can be classified into three discrete clades based on variations in the toxin domain of both effectors and their cognate immunity proteins (types I, II, and III) (Figure 5C). The GS086-type T6SS shared conserved delivery-related domains and variable effector domains. In addition to the variable toxin domains and the cognate immunity proteins, type II and III GS086-like T6SS V2 regions lack homologs of GS086_1896, confirming its irrelevancy in the effector's secretion (Figures 2E and 5C). Furthermore, several BtaeB and BtpeA homologs exhibited truncations (indicated by asterisks), while still retaining the domain associated with delivery (Figure 5C). The highly conserved delivery-related domains of two effectors (including $BtpeA_{D1}$ and $BtaeB_{400–407}$ loop), BtapC, and VgrG serving as essential assembly modules across all GS086-like T6SS V2 regions further support the crucial roles of BtapC in facilitating co-delivery of two effectors encoded in the *Bacteroides* T6SS V2 region (Figure 5C).

Further bioinformatics analysis revealed distinct effector distribution patterns within the GA3 T6SS V2 region (Figure 5D). Approximately 37.3% (606/1,623) of *B. fragilis* strains carry a single effector gene in this region, accounting for nearly half of all GA3 T6SS-positive isolates (Figure 5D). Moreover, a substantial proportion (>38%, 621/1,623) of *B. fragilis* strains (>50% of GA3 T6SS carriers) harbor two effectors in their V2 regions (Figure 5D). Beyond the GS086-type T6SS (13.7%, 223/1,623), both J38-type T6SS (17.6%, 285/1,623) and 1284-type T6SS (7.0%, 113/1,623) contain multiple uncharacterized proteins in their V2 regions, including two putative effectors (H1/H6 and h1/h6).[36] Notably, among functionally undefined proteins, H4/h4 proteins exhibit striking structural homology to BtapC, while the delivery domains of H1/h1 and H6/h6 show conserved features (Figures 5D and 5E). All these multi-effectors T6SS employ

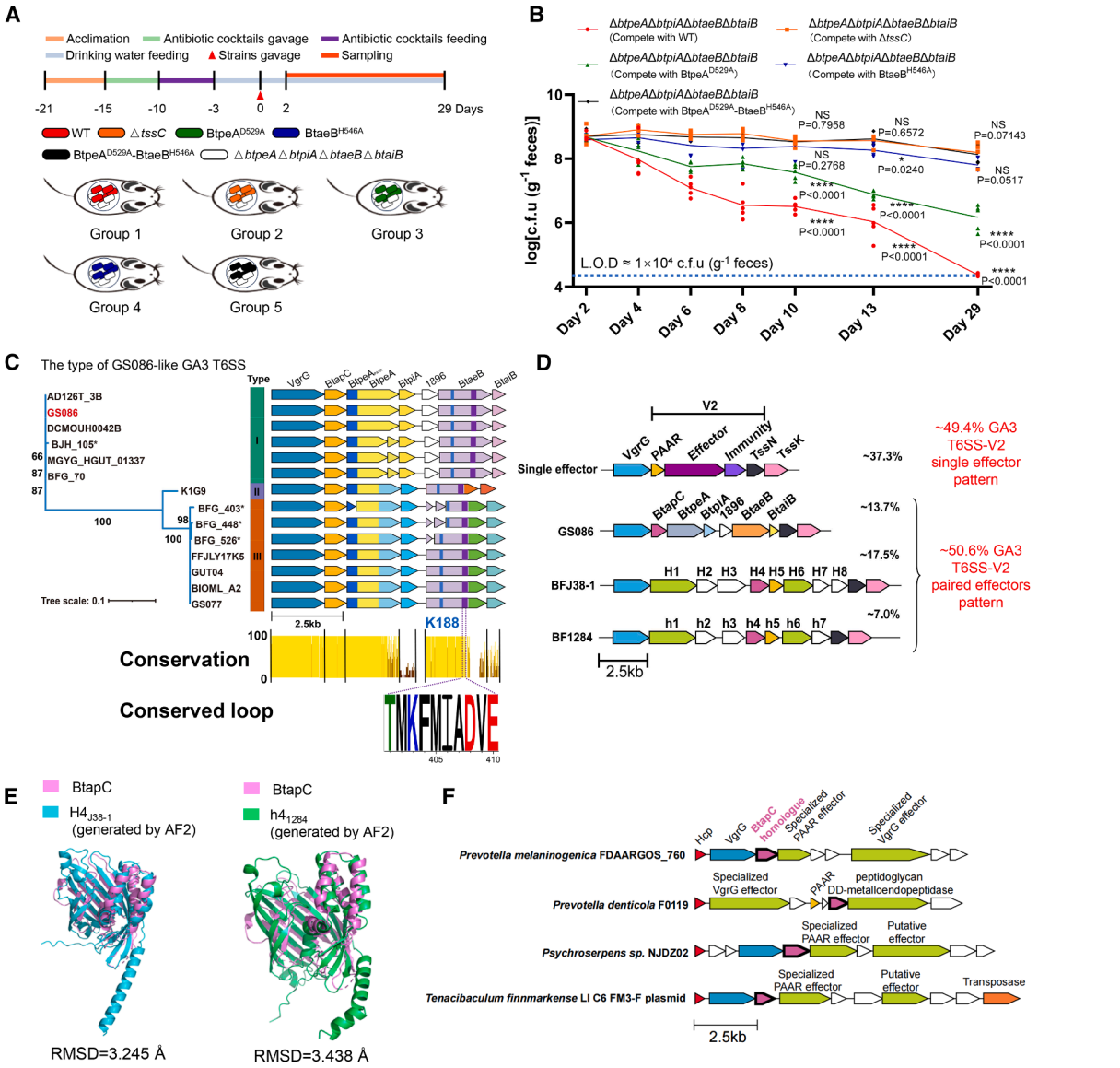

Figure 5. BtapC-mediated effector co-secretion renders a functional synergy in mice and is likely conserved in human gut Bacteroidota

(A) Schematic outline of antibiotic cocktail-treated and competitive colonization experiments in C57BL/6J mice. Numbers indicate days before (negative) and after (positive) gavage administration of strains.

(B) Competitive colonization experiments between donor (WT *B. fragilis* GS086 or isogenic deletion mutants) and recipient (GS086 isogenic sensitive mutant GS086Δ*btpeA*Δ*btpiA*Δ*btaeB*Δ*btaiB*) in antibiotic-treated C57BL/6J mice ($n = 5$ per group). Each dot represents an individual mice. Exact p values are indicated in the figure. The limit of detection in this competitive colonization experiment is about 1×10^4 CFU (g^{-1} feces).

(C) Maximum likelihood phylogenetic tree of the V2 region of the GS086-like GA3 T6SS showing separation into 3 subtypes. Bootstrap values (1,000 replicates) are clearly indicated at each branch node. Toxic domains of distinct subtypes of effectors and their cognate immunity proteins are depicted using varying colors. The height of the yellow block labeled with the identity value is used to indicate the conservation of each protein in the V2 region. The conserved $BtpeA_{PAAR}$ domain and the unique loop of BtaeB are respectively depicted in dark blue and dark purple. Sequence logos are generated from alignments of the unique loops associated with distinct subtypes of BtaeB.

(D) The heterogeneous effector distribution patterns in the V2 region of GA3 T6SS. The proportion of each V2 region within all publicly available *B. fragilis* genomes is indicated following the T6SS loci. The putative effectors are colored in green (H1/H6 and h1/h6). BtapC and BtapC homologs are colored in dark red. The hypothetical proteins are colored in white.

(E) Structural alignment of BtapC with $H4_{J38-1}$ or $h4_{1284}$. The $H4_{J38-1}$ and $h4_{1284}$ both exhibit significant structural similarity to BtapC.

(F) Schematic representation of BtapC homologs-containing T6SS loci in the selected Bacteroidota species. Unknown function proteins are colored in white, and putative effectors are colored in light green.

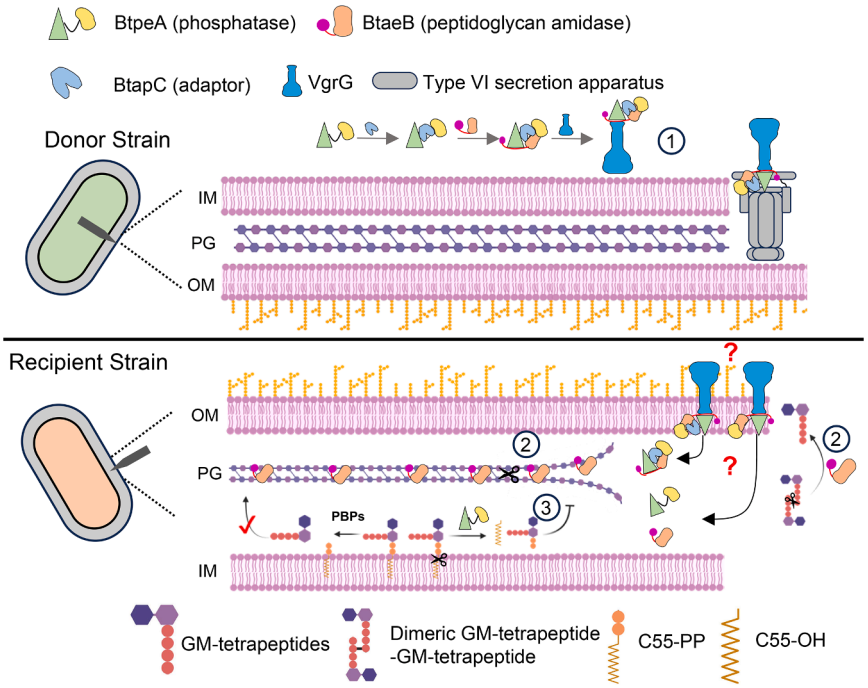

Figure 6. Proposed model for BtapC-mediated effector co-secretion

In donor strains, BtapC interacts with BtpeA, facilitating subsequent incorporation of BtaeB into the binary complex. The integration of BtaeB enables its unique loop (red curved line) insertion into the VgrG-BtpeA interaction interface, thereby stabilizing the VgrG-BtpeA-BtaeB-BtapC quaternary complex through multiple interaction networks (step 1, top). In recipient strains, the amidase BtaeB effectively degrades peptidoglycan (step 2). The phosphatase BtpeA targets the peptidoglycan precursor lipid II (step 3), thereby hindering the process of repairing damaged peptidoglycan (bottom).

a BtapC-mediated co-delivery mechanism, representing a conserved mechanism for coordinated effector secretion.

Comparative genomic analysis uncovered conserved BtapC-coordinated effector delivery systems throughout Bacteroidota lineages (Figure 5F), mediating the co-secretion of either independent or specialized effectors. Although BtapC homologs exhibit limited sequence conservation (11%–23% amino acid identity), they display conserved structural similarities across phylogenetically divergent Bacteroidota lineages (Figures S5E and S5F), reinforcing the biological importance of this multi-cargo delivery mechanism in microbial adaptation. Notably, we detected a BtapC-containing T6SS gene cluster residing on a plasmid with mobile genetic elements (MGEs) in *Tenacibaculum finnmarkense* (Figure 5F). The inherent horizontal transfer capacity of these plasmid-encoded MGEs likely facilitated the phylogenetic dissemination of BtapC-associated T6SS across divergent bacterial lineages, potentially contributing to its evolutionary success.

DISCUSSION

Here, we report the synergistic functionality of two effectors and effector-dependent secretion in *Bacteroides* T6SS. The amidase BtaeB degrades peptidoglycan in recipient strains, while the phosphatase BtpeA targets the peptidoglycan precursor lipid II, impeding damaged peptidoglycan repair (Figure 6). The combined activities of cell-wall destruction and repair interference synergistically enhance fitness in the gut ecosystem, surpassing individual effector effects. A recent study has reported that the T6SS can deliver multiple components (one effector and one adaptor) per secretion event, revealing effector translocation complexity.[55] Although the adaptor was referred to as a "co-effector" in the context, it should be noted that the authors specifically clarified that this component mediates effector delivery rather than functioning as an effector itself.

Based on the interaction between BtaeB and BtpeA in the presence of BtapC, along with the crucial role played by the unique loop of BtaeB in aiding BtpeA loading onto VgrG, we propose a putative assembly model for T6SS's "pre-firing" complex (Figure 6). This sophisticated co-delivery system involving both effectors ensures their simultaneous delivery via T6SS to recipient strains, enabling them to confer fitness advantages synergistically.

Interestingly, BtapC was detectable in whole-cell lysates but not in culture supernatants (Figures S6A and S6B). This finding, although unexpected given the structural stability of the VgrG-BtpeA-BtaeB-BtapC quaternary complex, is consistent with observations reported for other T6SS adaptor proteins.[56] In this case, BtapC would dissociate from the quaternary complex before injection, a process that may be facilitated by its interaction with T6SS membrane complex components or the T6SS baseplate. However, if BtapC is secreted, it may be prone to degradation, thereby stimulating the release of BtpeA and BtaeB in the periplasm of recipient cells. Key unresolved questions remain regarding whether BtapC is secreted or retained, and if the latter, how it is excluded from the stable quaternary complex during T6SS firing. Additional investigation is needed to determine the state of the VgrG-BtpeA-BtaeB-(BtapC) complex should it reach the periplasm of recipient cells.

Furthermore, our findings support the hypothesis that the absence of either effector, which compromises the antagonistic capabilities of the encoding strains, leads to failure of the PAAR domain to load onto VgrG and significantly reduces Hcp secretion. A previous study observed that effector absence only partially impaired T6SS secretion, with complete secretion loss requiring deleting all effectors.[24] By contrast, we show that deleting any single effector nearly abolishes secretion. Our findings reveal a unique checkpoint mechanism requiring both effectors' physical presence for T6SS assembly in *B. fragilis*, ensuring simultaneous loading/secretion of both effectors per firing. The regulation of T6SS assembly and firing by effectors is intriguing, as it maximizes effector loading and toxicity while preventing futile firing of T6SS components, thus conserving energy.

BtapC represents an unreported T6SS adaptor class with distinct structure, suggesting Bacteroidota evolved specialized

co-delivery systems (Figures 5F, S3C, S5E, and S5F). Bioinformatics analysis revealed that BtapC-encoded T6SS possesses conserved delivery-related components and variable effector domains, suggesting that *Bacteroides* T6SS has evolved a potential modular assembly strategy, characterized by consistent delivery domains fused with distinct toxic domains to effectively combat the intricate interbacterial competition environment (Figure 5C).

While earlier studies connect *Bacteroides* T6SS with early gut microbiota succession,[36] our antibiotic-treated model lacks this developmental context. Therefore, although our study identifies the BtapC-mediated dual effector co-delivery as functionally important and broadly applicable in *Bacteroides* competition *in vivo*, its relevance to natural infant microbiota colonization by T6SS still needs further study.

Overall, our research demonstrates that a conserved *Bacteroides* T6SS orchestrates the co-delivery of two effectors via BtapC, synergistically enhancing fitness via their combined activities. The presence of conserved delivery domains alongside variable toxic modules highlights the system's engineering potential, enabling the customization of toxic domains to enhance bactericidal efficacy/spectrum for targeted gut microbiome regulation.

RESOURCE AVAILABILITY

Lead contact

Further information and requests for resources and reagents should be directed to and will be fulfilled by the lead contact, Xiang Gao (xgao@email.sdu.edu.cn).

Materials availability

Plasmids and strains generated in this study are available from the lead contact under a materials transfer agreement with Shandong University.

Data and code availability

- X-ray crystallography data (PDB: 9JDI and 9JDH) and cryo-EM data (PDB: 9JG8; EMDB: EMD-61458) have been deposited in the Protein Databank (http://www.rcsb.org) and the Electron Microscopy Databank (https://www.ebi.ac.uk/pdbe/emdb/). All original code has been deposited at PDB and EMDB and is publicly available as of the date of publication. Accession numbers and DOIs are listed in the key resources table.
- This paper does not report original code.
- Any additional information required to reanalyze the data reported in this paper is available from the lead contact upon request.

ACKNOWLEDGMENTS

We thank members of the Gao laboratory for the insightful discussion. We thank the staff from the BL02U1 and BL10U2 beamlines of the National Facility for Protein Science Shanghai at SSRF for assistance during X-ray data collection. The cryo-EM data were collected at the Biomedical Research Center for Structural Analysis, Shandong University, and we thank Drs. Lei Qi and Dongfang He for their help during data collection. We are grateful to Dianli Zhao and Kang Li (cryo-EM facility for Marine Biology, Laoshan laboratory) for their assistance in cryo-EM sample screening. We also thank Xiangmei Ren, Jingyao Qu, Guannan Lin, Yuyu Guo, Sen Wang, Chengjia Zhang, Haiyan Sui, and Xiaoju Li from the Core Facilities for Life and Environmental Sciences and the SKLMT of Shandong University for their assistance in HPLC, laser-scanning confocal microscopy, TEM, and X-ray diffraction experiments. This study was supported by the National Key R&D Program of China (grant no. 2024YFA0920100 to X.G.), the National Natural Science Foundation of China (grant no. 323B2003 to W.L.), the Shandong Provincial Natural Science Foundation (grant no. ZR2024ZD47 to X.G.), the SKLMT Frontiers and Challenges Project (grant no. SKLMTFCP-2023-01), and the Intramural Joint Program Fund of the State Key Laboratory of Microbial Technology (grant no. SKLMTIJP-2025-01). Some elements in the figures were created in BioRender. Gao, X. (2025) https://BioRender.com/kphqy6n.

AUTHOR CONTRIBUTIONS

Conceptualization, X.G.; methodology, X.G., W.L., S.Z., X.X., J.H., X.J., M.W., W.H., S.L., X.J., and B.L.; investigation, W.L., S.Z., J.H., and X.J.; validation, W.L. and S.Z.; visualization, W.L. and S.Z.; writing – original draft, X.G., W.L., S.Z., X.J., B.L., and F.S.; writing – review & editing, X.G., W.L., S.Z., B.L., S.L., J.H., and F.S.; resources, X.G., M.W., W.H., and X.J.; funding acquisition, X.G. and W.L.; supervision, X.G.

DECLARATION OF INTERESTS

The authors declare no competing interests.

STAR★METHODS

Detailed methods are provided in the online version of this paper and include the following:

- KEY RESOURCES TABLE
- EXPERIMENTAL MODEL AND SUBJECT DETAILS
  - Bacterial strains and growth conditions
  - Animal experiments
- METHOD DETAILS
  - Plasmid construction
  - Protein expression and purification
  - Protein crystallization and structure determination
  - Cryo-EM sample preparation and data collection
  - Cryo-EM data processing
  - Model building into cryo-EM maps
  - Conjugation and resistance selection
  - *In situ* genetic manipulation in *Bacteroides*
  - Agar spot assay
  - Fluorescence microscopy
  - Co-culture/competition assay *in vitro*
  - Western immunoblot analysis
  - Co-immunoprecipitation and immunoblotting analysis
  - Pull-down assay
  - Phosphatase activity assay
  - Extraction of lipids from membrane fractions
  - HPLC analysis of membrane lipids
  - Preparation of peptidoglycan
  - Digestion of Peptidoglycan and HPLC analysis
  - Analysis of GS086-like type T6SS V2 region
  - Analysis of single or two effectors-containing T6SS V2 region
  - Analysis of BtapC-homologues in Bacteroidota Species
  - Structural similarity search
- QUANTIFICATION AND STATISTICAL ANALYSIS

SUPPLEMENTAL INFORMATION

Supplemental information can be found online at https://doi.org/10.1016/j.chom.2025.09.012.

Received: April 17, 2025
Revised: July 31, 2025
Accepted: September 15, 2025
Published: October 9, 2025

REFERENCES

1. García-Bayona, L., and Comstock, L.E. (2018). Bacterial antagonism in host-associated microbial communities. Science *361*, eaat2456. https://doi.org/10.1126/science.aat2456.
2. Jiang, K., Li, W., Tong, M., Xu, J., Chen, Z., Yang, Y., Zang, Y., Jiao, X., Liu, C., Lim, B., et al. (2024). *Bacteroides fragilis* ubiquitin homologue drives intraspecies bacterial competition in the gut microbiome. Nat. Microbiol. *9*, 70–84. https://doi.org/10.1038/s41564-023-01541-5.
3. Jiang, K., Pang, X., Li, W., Xu, X., Yang, Y., Shang, C., and Gao, X. (2025). Interbacterial warfare in the human gut: insights from Bacteroidales' perspective. Gut Microbes *17*, 2473522. https://doi.org/10.1080/19490976.2025.2473522.
4. Basler, M., Ho, B.T., and Mekalanos, J.J. (2013). Tit-for-tat: type VI secretion system counterattack during bacterial cell-cell interactions. Cell *152*, 884–894. https://doi.org/10.1016/j.cell.2013.01.042.
5. Russell, A.B., Singh, P., Brittnacher, M., Bui, N.K., Hood, R.D., Carl, M.A., Agnello, D.M., Schwarz, S., Goodlett, D.R., Vollmer, W., et al. (2012). A widespread bacterial type VI secretion effector superfamily identified using a heuristic approach. Cell Host Microbe *11*, 538–549. https://doi.org/10.1016/j.chom.2012.04.007.
6. Sibinelli-Sousa, S., Hespanhol, J.T., Nicastro, G.G., Matsuyama, B.Y., Mesnage, S., Patel, A., de Souza, R.F., Guzzo, C.R., and Bayer-Santos, E. (2020). A Family of T6SS Antibacterial Effectors Related to l,d-Transpeptidases Targets the Peptidoglycan. Cell Rep. *31*, 107813. https://doi.org/10.1016/j.celrep.2020.107813.
7. Russell, A.B., LeRoux, M., Hathazi, K., Agnello, D.M., Ishikawa, T., Wiggins, P.A., Wai, S.N., and Mougous, J.D. (2013). Diverse type VI secretion phospholipases are functionally plastic antibacterial effectors. Nature *496*, 508–512. https://doi.org/10.1038/nature12074.
8. González-Magaña, A., Altuna, J., Queralt-Martín, M., Largo, E., Velázquez, C., Montánchez, I., Bernal, P., Alcaraz, A., and Albesa-Jové, D. (2022). The *P. aeruginosa* effector Tse5 forms membrane pores disrupting the membrane potential of intoxicated bacteria. Commun. Biol. *5*, 1189. https://doi.org/10.1038/s42003-022-04140-y.
9. Whitney, J.C., Quentin, D., Sawai, S., LeRoux, M., Harding, B.N., Ledvina, H.E., Tran, B.Q., Robinson, H., Goo, Y.A., Goodlett, D.R., et al. (2015). An interbacterial NAD(P)(+) glycohydrolase toxin requires elongation factor Tu for delivery to target cells. Cell *163*, 607–619. https://doi.org/10.1016/j.cell.2015.09.027.
10. de Moraes, M.H., Hsu, F., Huang, D., Bosch, D.E., Zeng, J., Radey, M.C., Simon, N., Ledvina, H.E., Frick, J.P., Wiggins, P.A., et al. (2021). An interbacterial DNA deaminase toxin directly mutagenizes surviving target populations. eLife *10*, e62967. https://doi.org/10.7554/eLife.62967.
11. Ahmad, S., Wang, B., Walker, M.D., Tran, H.R., Stogios, P.J., Savchenko, A., Grant, R.A., McArthur, A.G., Laub, M.T., and Whitney, J.C. (2019). An interbacterial toxin inhibits target cell growth by synthesizing (p)ppApp. Nature *575*, 674–678. https://doi.org/10.1038/s41586-019-1735-9.
12. Whitney, J.C., Beck, C.M., Goo, Y.A., Russell, A.B., Harding, B.N., De Leon, J.A., Cunningham, D.A., Tran, B.Q., Low, D.A., Goodlett, D.R., et al. (2014). Genetically distinct pathways guide effector export through the type VI secretion system. Mol. Microbiol. *92*, 529–542. https://doi.org/10.1111/mmi.12571.
13. Howard, S.A., Furniss, R.C.D., Bonini, D., Amin, H., Paracuellos, P., Zlotkin, D., Costa, T.R.D., Levy, A., Mavridou, D.A.I., and Filloux, A. (2021). The Breadth and Molecular Basis of Hcp-Driven Type VI Secretion System Effector Delivery. mBio *12*, e0026221. https://doi.org/10.1128/mBio.00262-21.
14. Flaugnatti, N., Rapisarda, C., Rey, M., Beauvois, S.G., Nguyen, V.A., Canaan, S., Durand, E., Chamot-Rooke, J., Cascales, E., Fronzes, R., et al. (2020). Structural basis for loading and inhibition of a bacterial T6SS phospholipase effector by the VgrG spike. EMBO J. *39*, e104129. https://doi.org/10.15252/embj.2019104129.
15. Shneider, M.M., Buth, S.A., Ho, B.T., Basler, M., Mekalanos, J.J., and Leiman, P.G. (2013). PAAR-repeat proteins sharpen and diversify the type VI secretion system spike. Nature *500*, 350–353. https://doi.org/10.1038/nature12453.
16. Burkinshaw, B.J., Liang, X., Wong, M., Le, A.N.H., Lam, L., and Dong, T.G. (2018). A type VI secretion system effector delivery mechanism dependent on PAAR and a chaperone-co-chaperone complex. Nat. Microbiol. *3*, 632–640. https://doi.org/10.1038/s41564-018-0144-4.
17. Unterweger, D., Kostiuk, B., Ötjengerdes, R., Wilton, A., Diaz-Satizabal, L., and Pukatzki, S. (2015). Chimeric adaptor proteins translocate diverse type VI secretion system effectors in Vibrio cholerae. EMBO J. *34*, 2198–2210. https://doi.org/10.15252/embj.201591163.
18. Liang, X., Moore, R., Wilton, M., Wong, M.J.Q., Lam, L., and Dong, T.G. (2015). Identification of divergent type VI secretion effectors using a conserved chaperone domain. Proc. Natl. Acad. Sci. USA *112*, 9106–9111. https://doi.org/10.1073/pnas.1505317112.
19. Pukatzki, S., Ma, A.T., Revel, A.T., Sturtevant, D., and Mekalanos, J.J. (2007). Type VI secretion system translocates a phage tail spike-like protein into target cells where it cross-links actin. Proc. Natl. Acad. Sci. USA *104*, 15508–15513. https://doi.org/10.1073/pnas.0706532104.
20. Quentin, D., Ahmad, S., Shanthamoorthy, P., Mougous, J.D., Whitney, J.C., and Raunser, S. (2018). Mechanism of loading and translocation of type VI secretion system effector Tse6. Nat. Microbiol. *3*, 1142–1152. https://doi.org/10.1038/s41564-018-0238-z.
21. Ma, J., Pan, Z., Huang, J., Sun, M., Lu, C., and Yao, H. (2017). The Hcp proteins fused with diverse extended-toxin domains represent a novel pattern of antibacterial effectors in type VI secretion systems. Virulence *8*, 1189–1202. https://doi.org/10.1080/21505594.2017.1279374.
22. Silverman, J.M., Agnello, D.M., Zheng, H., Andrews, B.T., Li, M., Catalano, C.E., Gonen, T., and Mougous, J.D. (2013). Haemolysin coregulated protein is an exported receptor and chaperone of type VI secretion substrates. Mol. Cell *51*, 584–593. https://doi.org/10.1016/j.molcel.2013.07.025.
23. Bondage, D.D., Lin, J.S., Ma, L.S., Kuo, C.H., and Lai, E.M. (2016). VgrG C terminus confers the type VI effector transport specificity and is required for binding with PAAR and adaptor-effector complex. Proc. Natl. Acad. Sci. USA *113*, E3931–E3940. https://doi.org/10.1073/pnas.1600428113.
24. Liang, X., Kamal, F., Pei, T.-T., Xu, P., Mekalanos, J.J., and Dong, T.G. (2019). An onboard checking mechanism ensures effector delivery of the type VI secretion system in *Vibrio cholerae*. Proc. Natl. Acad. Sci. USA *116*, 23292–23298. https://doi.org/10.1073/pnas.1914202116.
25. LaCourse, K.D., Peterson, S.B., Kulasekara, H.D., Radey, M.C., Kim, J., and Mougous, J.D. (2018). Conditional toxicity and synergy drive diversity among antibacterial effectors. Nat. Microbiol. *3*, 440–446. https://doi.org/10.1038/s41564-018-0113-y.
26. Rudzite, M., Subramoni, S., Endres, R.G., and Filloux, A. (2023). Effectiveness of *Pseudomonas aeruginosa* type VI secretion system relies on toxin potency and type IV pili-dependent interaction. PLoS Pathog. *19*, e1011428. https://doi.org/10.1371/journal.ppat.1011428.
27. Jana, B., Keppel, K., Fridman, C.M., Bosis, E., and Salomon, D. (2022). Multiple T6SSs, Mobile Auxiliary Modules, and Effectors Revealed in a Systematic Analysis of the *Vibrio parahaemolyticus* Pan-Genome. mSystems *7*, e0072322. https://doi.org/10.1128/msystems.00723-22.
28. Ma, L.S., Hachani, A., Lin, J.S., Filloux, A., and Lai, E.M. (2014). *Agrobacterium tumefaciens* deploys a superfamily of type VI secretion DNase effectors as weapons for interbacterial competition in planta. Cell Host Microbe *16*, 94–104. https://doi.org/10.1016/j.chom.2014.06.002.
29. Russell, A.B., Wexler, A.G., Harding, B.N., Whitney, J.C., Bohn, A.J., Goo, Y.A., Tran, B.Q., Barry, N.A., Zheng, H., Peterson, S.B., et al. (2014). A type VI secretion-related pathway in Bacteroidetes mediates interbacterial antagonism. Cell Host Microbe *16*, 227–236. https://doi.org/10.1016/j.chom.2014.07.007.
30. Coyne, M.J., Roelofs, K.G., and Comstock, L.E. (2016). Type VI secretion systems of human gut Bacteroidales segregate into three genetic architectures, two of which are contained on mobile genetic elements. BMC Genomics *17*, 58. https://doi.org/10.1186/s12864-016-2377-z.

31. Chatzidaki-Livanis, M., Geva-Zatorsky, N., and Comstock, L.E. (2016). *Bacteroides fragilis* type VI secretion systems use novel effector and immunity proteins to antagonize human gut Bacteroidales species. Proc. Natl. Acad. Sci. USA *113*, 3627–3632. https://doi.org/10.1073/pnas.1522510113.

32. Wexler, A.G., Bao, Y., Whitney, J.C., Bobay, L.M., Xavier, J.B., Schofield, W.B., Barry, N.A., Russell, A.B., Tran, B.Q., Goo, Y.A., et al. (2016). Human symbionts inject and neutralize antibacterial toxins to persist in the gut. Proc. Natl. Acad. Sci. USA *113*, 3639–3644. https://doi.org/10.1073/pnas.1525637113.

33. Hecht, A.L., Casterline, B.W., Earley, Z.M., Goo, Y.A., Goodlett, D.R., and Bubeck Wardenburg, J. (2016). Strain competition restricts colonization of an enteric pathogen and prevents colitis. EMBO Rep. *17*, 1281–1291. https://doi.org/10.15252/embr.201642282.

34. Lim, B., Xu, J., Wierzbicki, I.H., Gonzalez, C.G., Chen, Z., Gonzalez, D.J., Gao, X., and Goodman, A.L. (2025). A human gut bacterium antagonizes neighboring bacteria by altering their protein-folding ability. Cell Host Microbe *33*, 200–217.e24. https://doi.org/10.1016/j.chom.2025.01.008.

35. Ross, B.D., Verster, A.J., Radey, M.C., Schmidtke, D.T., Pope, C.E., Hoffman, L.R., Hajjar, A.M., Peterson, S.B., Borenstein, E., and Mougous, J.D. (2019). Human gut bacteria contain acquired interbacterial defence systems. Nature *575*, 224–228. https://doi.org/10.1038/s41586-019-1708-z.

36. Verster, A.J., Ross, B.D., Radey, M.C., Bao, Y., Goodman, A.L., Mougous, J.D., and Borenstein, E. (2017). The Landscape of Type VI Secretion across Human Gut Microbiomes Reveals Its Role in Community Composition. Cell Host Microbe *22*, 411–419.e4. https://doi.org/10.1016/j.chom.2017.08.010.

37. García-Bayona, L., Coyne, M.J., and Comstock, L.E. (2021). Mobile Type VI secretion system loci of the gut Bacteroidales display extensive intra-ecosystem transfer, multi-species spread and geographical clustering. PLoS Genet. *17*, e1009541. https://doi.org/10.1371/journal.pgen.1009541.

38. Coyne, M.J., and Comstock, L.E. (2019). Type VI Secretion Systems and the Gut Microbiota. Microbiol. Spectr. *7*, 1–7. https://doi.org/10.1128/microbiolspec.PSIB-0009-2018.

39. Almagro Armenteros, J.J., Tsirigos, K.D., Sønderby, C.K., Petersen, T.N., Winther, O., Brunak, S., von Heijne, G., and Nielsen, H. (2019). SignalP 5.0 improves signal peptide predictions using deep neural networks. Nat. Biotechnol. *37*, 420–423. https://doi.org/10.1038/s41587-019-0036-z.

40. Potter, S.C., Luciani, A., Eddy, S.R., Park, Y., Lopez, R., and Finn, R.D. (2018). HMMER web server: 2018 update. Nucleic Acids Res. *46*, W200–W204. https://doi.org/10.1093/nar/gky448.

41. Blum, M., Andreeva, A., Florentino, L.C., Chuguransky, S.R., Grego, T., Hobbs, E., Pinto, B.L., Orr, A., Paysan-Lafosse, T., Ponamareva, I., et al. (2025). InterPro: the protein sequence classification resource in 2025. Nucleic Acids Res. *53*, D444–D456. https://doi.org/10.1093/nar/gkae1082.

42. Holm, L. (2022). Dali server: structural unification of protein families. Nucleic Acids Res. *50*, W210–W215. https://doi.org/10.1093/nar/gkac387.

43. Barreteau, H., Bouhss, A., Gérard, F., Duché, D., Boussaid, B., Blanot, D., Lloubès, R., Mengin-Lecreulx, D., and Touzé, T. (2010). Deciphering the catalytic domain of colicin M, a peptidoglycan lipid II-degrading enzyme. J. Biol. Chem. *285*, 12378–12389. https://doi.org/10.1074/jbc.M109.093583.

44. Grinter, R., Roszak, A.W., Cogdell, R.J., Milner, J.J., and Walker, D. (2012). The crystal structure of the lipid II-degrading bacteriocin syringacin M suggests unexpected evolutionary relationships between colicin M-like bacteriocins. J. Biol. Chem. *287*, 38876–38888. https://doi.org/10.1074/jbc.M112.400150.

45. Zeth, K., Römer, C., Patzer, S.I., and Braun, V. (2008). Crystal structure of colicin M, a novel phosphatase specifically imported by *Escherichia coli*. J. Biol. Chem. *283*, 25324–25331. https://doi.org/10.1074/jbc.M802591200.

46. Egan, A.J.F., Errington, J., and Vollmer, W. (2020). Regulation of peptidoglycan synthesis and remodelling. Nat. Rev. Microbiol. *18*, 446–460. https://doi.org/10.1038/s41579-020-0366-3.

47. Beis, K., and Rebuffat, S. (2019). Multifaceted ABC transporters associated to microcin and bacteriocin export. Res. Microbiol. *170*, 399–406. https://doi.org/10.1016/j.resmic.2019.07.002.

48. Desmarais, S.M., De Pedro, M.A., Cava, F., and Huang, K.C. (2013). Peptidoglycan at its peaks: how chromatographic analyses can reveal bacterial cell wall structure and assembly. Mol. Microbiol. *89*, 1–13. https://doi.org/10.1111/mmi.12266.

49. He, W., Wu, K., Ouyang, Z., Bai, Y., Luo, W., Wu, D., An, H., Guo, Y., Jiao, M., Qin, Q., et al. (2023). Structure and assembly of type VI secretion system cargo delivery vehicle. Cell Rep. *42*, 112781. https://doi.org/10.1016/j.celrep.2023.112781.

50. Cianfanelli, F.R., Alcoforado Diniz, J., Guo, M., De Cesare, V., Trost, M., and Coulthurst, S.J. (2016). VgrG and PAAR Proteins Define Distinct Versions of a Functional Type VI Secretion System. PLoS Pathog. *12*, e1005735. https://doi.org/10.1371/journal.ppat.1005735.

51. Colautti, J., Tan, H., Bullen, N.P., Thang, S.S., Hackenberger, D., Doxey, A.C., and Whitney, J.C. (2024). A widespread accessory protein family diversifies the effector repertoire of the type VI secretion system spike. Nat. Commun. *15*, 10108. https://doi.org/10.1038/s41467-024-54509-2.

52. Ahmad, S., Tsang, K.K., Sachar, K., Quentin, D., Tashin, T.M., Bullen, N.P., Raunser, S., McArthur, A.G., Prehna, G., and Whitney, J.C. (2020). Structural basis for effector transmembrane domain recognition by type VI secretion system chaperones. eLife *9*, e62816. https://doi.org/10.7554/eLife.62816.

53. Sachar, K., Kanarek, K., Colautti, J., Kim, Y., Bosis, E., Prehna, G., Salomon, D., and Whitney, J.C. (2025). A conserved chaperone protein is required for the formation of a noncanonical type VI secretion system spike tip complex. J. Biol. Chem. *301*, 108242. https://doi.org/10.1016/j.jbc.2025.108242.

54. Jamali, K., Käll, L., Zhang, R., Brown, A., Kimanius, D., and Scheres, S.H.W. (2024). Automated model building and protein identification in cryo-EM maps. Nature *628*, 450–457. https://doi.org/10.1038/s41586-024-07215-4.

55. Dar, Y., Jana, B., Bosis, E., and Salomon, D. (2022). A binary effector module secreted by a type VI secretion system. EMBO Rep. *23*, e53981. https://doi.org/10.15252/embr.202153981.

56. Unterweger, D., Kostiuk, B., and Pukatzki, S. (2017). Adaptor Proteins of Type VI Secretion System Effectors. Trends Microbiol. *25*, 8–10. https://doi.org/10.1016/j.tim.2016.10.003.

57. Lim, B., Zimmermann, M., Barry, N.A., and Goodman, A.L. (2017). Engineered Regulatory Systems Modulate Gene Expression of Human Commensals in the Gut. Cell *169*, 547–558.e15. https://doi.org/10.1016/j.cell.2017.03.045.

58. Tong, M., Xu, J., Li, W., Jiang, K., Yang, Y., Chen, Z., Jiao, X., Meng, X., Wang, M., Hong, J., et al. (2024). A highly conserved SusCD transporter determines the import and species-specific antagonism of Bacteroides ubiquitin homologues. Nat. Commun. *15*, 8794. https://doi.org/10.1038/s41467-024-53149-w.

59. Bencivenga-Barry, N.A., Lim, B., Herrera, C.M., Trent, M.S., and Goodman, A.L. (2020). Genetic Manipulation of Wild Human Gut *Bacteroides*. J. Bacteriol. *202*, e00544-19. https://doi.org/10.1128/JB.00544-19.

60. Emsley, P., and Cowtan, K. (2004). Coot: model-building tools for molecular graphics. Acta Crystallogr. D Biol. Crystallogr. *60*, 2126–2132. https://doi.org/10.1107/S0907444904019158.

61. Meng, E.C., Goddard, T.D., Pettersen, E.F., Couch, G.S., Pearson, Z.J., Morris, J.H., and Ferrin, T.E. (2023). UCSF ChimeraX: Tools for structure building and analysis. Protein Sci. *32*, e4792. https://doi.org/10.1002/pro.4792.

62. Punjani, A., Rubinstein, J.L., Fleet, D.J., and Brubaker, M.A. (2017). cryoSPARC: algorithms for rapid unsupervised cryo-EM structure determination. Nat. Methods *14*, 290–296. https://doi.org/10.1038/nmeth.4169.

63. Liebschner, D., Afonine, P.V., Baker, M.L., Bunkóczi, G., Chen, V.B., Croll, T.I., Hintze, B., Hung, L.W., Jain, S., McCoy, A.J., et al. (2019). Macromolecular structure determination using X-rays, neutrons and

electrons: recent developments in Phenix. Acta Crystallogr. D Struct. Biol. *75*, 861–877. https://doi.org/10.1107/S2059798319011471.

64. Camacho, C., Coulouris, G., Avagyan, V., Ma, N., Papadopoulos, J., Bealer, K., and Madden, T.L. (2009). BLAST+: architecture and applications. BMC Bioinf. *10*, 421. https://doi.org/10.1186/1471-2105-10-421.

65. Katoh, K., and Standley, D.M. (2013). MAFFT multiple sequence alignment software version 7: improvements in performance and usability. Mol. Biol. Evol. *30*, 772–780. https://doi.org/10.1093/molbev/mst010.

66. Minh, B.Q., Schmidt, H.A., Chernomor, O., Schrempf, D., Woodhams, M. D., von Haeseler, A., and Lanfear, R. (2020). IQ-TREE 2: New Models and Efficient Methods for Phylogenetic Inference in the Genomic Era. Mol. Biol. Evol. *37*, 1530–1534. https://doi.org/10.1093/molbev/msaa015.

67. Gilchrist, C.L.M., and Chooi, Y.H. (2021). clinker & clustermap.js: automatic generation of gene cluster comparison figures. Bioinformatics *37*, 2473–2475. https://doi.org/10.1093/bioinformatics/btab007.

68. Gibson, D.G., Young, L., Chuang, R.-Y., Venter, J.C., Hutchison, C.A., and Smith, H.O. (2009). Enzymatic assembly of DNA molecules up to several hundred kilobases. Nat. Methods *6*, 343–345. https://doi.org/10.1038/nmeth.1318.

69. Liu, H., and Naismith, J.H. (2008). An efficient one-step site-directed deletion, insertion, single and multiple-site plasmid mutagenesis protocol. BMC Biotechnol. *8*, 91. https://doi.org/10.1186/1472-6750-8-91.

70. García-Bayona, L., and Comstock, L.E. (2019). Streamlined Genetic Manipulation of Diverse *Bacteroides* and *Parabacteroides* Isolates from the Human Gut Microbiota. mBio *10*, e01762-19. https://doi.org/10.1128/mBio.01762-19.

71. Jiang, K., Chen, Z., Shi, Y., Zang, Y., Shang, C., Huang, X., Zang, J., Bai, Z., Jiao, X., Cai, J., et al. (2023). A strategy to enhance the insecticidal potency of Vip3Aa by introducing additional cleavage sites to increase its proteolytic activation efficiency. Eng. Microbiol. *3*, 100083. https://doi.org/10.1016/j.engmic.2023.100083.

72. Yu, F., Wang, Q., Li, M., Zhou, H., Liu, K., Zhang, K., Wang, Z., Xu, Q., Xu, C., Pan, Q., et al. (2019). *Aquarium*: an automatic data-processing and experiment information management system for biological macromolecular crystallography beamlines. J. Appl. Crystallogr. *52*, 472–477. https://doi.org/10.1107/S1600576719001183.

73. Jumper, J., Evans, R., Pritzel, A., Green, T., Figurnov, M., Ronneberger, O., Tunyasuvunakool, K., Bates, R., Žídek, A., Potapenko, A., et al. (2021). Highly accurate protein structure prediction with AlphaFold. Nature *596*, 583–589. https://doi.org/10.1038/s41586-021-03819-2.

74. Sit, B., Srisuknimit, V., Bueno, E., Zingl, F.G., Hullahalli, K., Cava, F., and Waldor, M.K. (2023). Undecaprenyl phosphate translocases confer conditional microbial fitness. Nature *613*, 721–728. https://doi.org/10.1038/s41586-022-05569-1.

75. Barreteau, H., Magnet, S., El Ghachi, M., Touzé, T., Arthur, M., Mengin-Lecreulx, D., and Blanot, D. (2009). Quantitative high-performance liquid chromatography analysis of the pool levels of undecaprenyl phosphate and its derivatives in bacterial membranes. J. Chromatogr. B Analyt. Technol. Biomed. Life Sci. *877*, 213–220. https://doi.org/10.1016/j.jchromb.2008.12.010.

76. Schaub, R.E., Chan, Y.A., Lee, M., Hesek, D., Mobashery, S., and Dillard, J.P. (2016). Lytic transglycosylases LtgA and LtgD perform distinct roles in remodeling, recycling and releasing peptidoglycan in Neisseria gonorrhoeae. Mol. Microbiol. *102*, 865–881. https://doi.org/10.1111/mmi.13496.

77. Zhao, L., Yin, G., Zhang, Y., Duan, C., Wang, Y., and Kang, Z. (2022). A comparative study on the genomes, transcriptomes, and metabolic properties of *Escherichia coli* strains Nissle 1917, BL21(DE3), and MG1655. Eng. Microbiol. *2*, 100012. https://doi.org/10.1016/j.engmic.2022.100012.

STAR★METHODS

KEY RESOURCES TABLE

REAGENT or RESOURCE	SOURCE	IDENTIFIER
Antibodies		
Rabbit polyclonal anti BtpeA	AtaGenix	N/A
Rabbit polyclonal anti BtaeB	AtaGenix	N/A
Rabbit polyclonal anti BtapC	AtaGenix	N/A
Rabbit polyclonal anti Hcp1	AtaGenix	N/A
Rabbit polyclonal anti DnaK	Cusabio	Cat# CSB-PA633459HA01EGW
Mouse monoclonal anti-Strepp-tag II	MBL	Cat# M211-3
Mouse monoclonal anti-HA-tag	MBL	Cat# M180-3; RRID: AB_10951811
Goat polyclonal anti-rabbit-HRP	MBL	Cat# 458; RRID: AB_2827722
Goat polyclonal anti-mouse-HRP	MBL	Cat# 330; RRID: AB_2650507
Bacterial and virus strains		
Bacteroides fragilis GS086	Lab collection	N/A
Bacteroides fragilis GS086-CmR	This paper	N/A
Bacteroides fragilis GS086Δ*tssC*	This paper	N/A
Bacteroides fragilis GS086Δ*btpeA*	This paper	N/A
Bacteroides fragilis GS086Δ*btpeA*:: P_{rhaR}-*btpeA*	This paper	N/A
Bacteroides fragilis GS086Δ*btpeA*$_{1\text{-}155\ aa}$	This paper	N/A
Bacteroides fragilis GS086Δ*btpeA*$_{156\text{-}end\ aa}$	This paper	N/A
Bacteroides fragilis GS086-BtepA^{D529A}	This paper	N/A
Bacteroides fragilis GS086Δ*btaeB*	This paper	N/A
Bacteroides fragilis GS086Δ*btaeB*:: P_{rhaR}-*btaeB*	This paper	N/A
Bacteroides fragilis GS086Δ*btaeB*$_{401\text{-}end\ aa}$	This paper	N/A
Bacteroides fragilis GS086Δ*btaeB*$_{411\text{-}end\ aa}$	This paper	N/A
Bacteroides fragilis GS086-BtaeB^{H546A}	This paper	N/A
Bacteroides fragilis GS086-BtepA^{D529A}BtaeB^{H546A}	This paper	N/A
Bacteroides fragilis GS086-BtepA^{D529A}BtaeB^{H546A}-Δ*btpiA*	This paper	N/A
Bacteroides fragilis GS086-BtepA^{D529A}BtaeB^{H546A}-Δ*btaiB*	This paper	N/A
Bacteroides fragilis GS086-BtepA^{D529A}BtaeB^{H546A}-Δ*btpiA*Δ*btaiB*	This paper	N/A
Bacteroides fragilis GS086Δ*btpeA* Δ*btaeB*	This paper	N/A
Bacteroides fragilis GS086Δ*btpeA* Δ*btpiA* Δ*btaeB* Δ*btaiB*	This paper	N/A
Bacteroides fragilis GS086Δ*btpeA* Δ*btpiA* Δ*btaeB* Δ*btaiB*-CmR	This paper	N/A
Bacteroides fragilis GS086Δ*btpeA* Δ*btpiA* Δ*btaeB* Δ*btaiB*:: P_{TonB3}-*btpiA*	This paper	N/A
Bacteroides fragilis GS086Δ*btpeA* Δ*btpiA* Δ*btaeB* Δ*btaiB*:: P_{TonB3}-*btaiB*	This paper	N/A
Bacteroides fragilis GS086Δ*btapC*	This paper	N/A
Bacteroides fragilis GS086Δ*btapC*::P_{TonB3}-*btapC*$^{HA\text{-}HIS}$	This paper	N/A
Bacteroides fragilis GS086-^{Strep}*vgrG*	This paper	N/A

(*Continued on next page*)

Continued

REAGENT or RESOURCE	SOURCE	IDENTIFIER
Bacteroides fragilis GS086- ^{Strep}*vgrG*/*btapC*^{HA}	This paper	N/A
Bacteroides fragilis GS086- ^{Strep}*vgrG*/*btapC*^{HA}-Δ*btpeA*	This paper	N/A
Bacteroides fragilis GS086- ^{Strep}*vgrG*/*btapC*^{HA}-Δ*btpeA*$_{1\text{-}155\ aa}$	This paper	N/A
Bacteroides fragilis GS086- ^{Strep}*vgrG*/*btapC*^{HA}-Δ*btpeA*$_{156\text{-}end\ aa}$	This paper	N/A
Bacteroides fragilis GS086- ^{Strep}*vgrG*/*btapC*^{HA}-Δ*btaeB*	This paper	N/A
Bacteroides fragilis GS086- ^{Strep}*vgrG*/*btapC*^{HA}-Δ*btaeB*$_{401\text{-}end\ aa}$	This paper	N/A
Bacteroides fragilis GS086- ^{Strep}*vgrG*/*btapC*^{HA}-Δ*btaeB*$_{411\text{-}end\ aa}$	This paper	N/A
Bacteroides xylanisolvens AM54-2NS	Lab collection	N/A
Bacteroides xylanisolvens::P$_{TonB3}$-*bfi1*$_{GS086}$	This paper	N/A
Bacteroides fragilis NCTC 9343	ATCC	25285
Bacteroides fragilis NCTC 9343:: P1T$_{DP}^{GH023}$-*btaeB*	This paper	N/A
Bacteroides fragilis NCTC 9343:: P1T$_{DP}^{GH023}$-*ss-btaeB*	This paper	N/A
Bacteroides fragilis NCTC 9343:: P1T$_{DP}^{GH023}$-*ss-btaeB*^{C460A}	This paper	N/A
Bacteroides fragilis NCTC 9343:: P1T$_{DP}^{GH023}$-*ss-btaeB*^{H546A}	This paper	N/A
Bacteroides fragilis NCTC 9343:: P1T$_{DP}^{GH023}$-*ss-btaeB-btaiB*	This paper	N/A
Escherichia coli MG1655	ATCC	700926
Escherichia coli BL21(DE3)	Thermo Fisher Scientific	Cat# EC0114
Escherichia coli S17-1 lambda pir	ATCC	BAA-2428
Chemicals, peptides, and recombinant proteins		
Brain Heart Infusion broth	HopeBio	Cat# HB8297-5
Luria-Bertani broth	BD Biosciences	Cat# 244620
Agar, Powder	Solarbio	Cat# A8190
Hemin	Sigma Aldrich	Cat# 51280
L-Cysteine	Solarbio	Cat# C0012
Critical commercial assays		
TIANprep Mini Plasmid Kit	TIANGEN	Cat# DP103-03
Universal DNA Purification Kit	TIANGEN	Cat# DP214
BCIP/NBT Premixed solution	Biosharp	Cat# BL709A
ClonExpress Ultra One Step Cloning Kit V2	Vazyme	Cat# C116-01
Ni-NTA agarose resin	QIAGEN	Cat# 30250
Strep-Tactin Sepharose resin	IBA Life Sciences	Cat# 2-1201-010
Strep-Tactin 4Flow High Capacity Resin	IBA Life Sciences	Cat# 2-1206-025
Anti-HA Nanobody Magarose Beads	AlpaLifeBio	Cat# KTSM1335
HiTrap Q	Cytiva	Cat# 17115401
Superdex 200 Increase 10/300 GL	Cytiva	Cat# 2899094
M5 Hiper ECL Western HRP Substrate	Mei5Bio	Cat# MF074-05
Deposited data		
Structure of BtpeA$_{251\text{-}end}$-BtpiA$_{19\text{-}end}$ Complex	This paper	PDB: 9JDI

(*Continued on next page*)

Continued

REAGENT or RESOURCE	SOURCE	IDENTIFIER
Structure of $BtaeB_{8\text{-}387}$	This paper	PDB: 9JDH
Structure of $VgrG_{570\text{-}618}$-$BtpeA_{2\text{-}156}$-$BtaeB1_{30\text{-}407}$-$BtapC_{6\text{-}243}$	This paper	PDB: 9JG8
EM data of $VgrG_{570\text{-}618}$-$BtpeA_{2\text{-}156}$-$BtaeB1_{30\text{-}407}$-$BtapC_{6\text{-}243}$	This paper	EMDB: EMD-61458
Experimental models: Organisms/strains		
Mouse: wild-type C57BL/6J (specific-pathogen-free level)	GemPharmatech Co., Ltd.	N/A
Oligonucleotides		
pNBU2-ss-line-F: tgacccgggctgcaggaa	Sangon	N/A
pNBU2-ss-line-R: gccggcaaatgagaactgtatag	Sangon	N/A
pSIE-CmR-*RS10745*-line-F: atgtggcctattgtttttacgc	Sangon	N/A
pSIE-CmR-*RS10745*-line-R: gcaactgtaaatgtcatctgatac	Sangon	N/A
T7-CP-F: gaaattaatacgactcactatag	Sangon	N/A
T7t-CP-R: aaacccctcaagacccgttt	Sangon	N/A
CmR-CP-F: aagcacaagttttatccggc	Sangon	N/A
CmR-CP-R: catggaagccatcacagacg	Sangon	N/A
RS10745-CS-CP-F: aaaggtttatccgctgtagc	Sangon	N/A
RS10745-CS-CP-R: tccttgcttcttccgaaatc	Sangon	N/A
Recombinant DNA		
pET15b vector	Novagen	Cat# 69661-3
pET15b-6HIS-SUMO-*btpeA*-AmpR	This paper	N/A
pET15b-6HIS-SUMO-$btpeA_{1\text{-}155\ aa}$-AmpR	This paper	N/A
pET15b-6HIS-SUMO-$btpeA_{156\text{-}250\ aa}$-AmpR	This paper	N/A
pET15b-6HIS-SUMO-$btpeA_{1\text{-}250\ aa}$-AmpR	This paper	N/A
pET15b-6HIS-SUMO-$btpeA_{251\text{-end aa}}$-AmpR	This paper	N/A
pET15b-6HIS-SUMO-$btpeA^{H434A}$-AmpR	This paper	N/A
pET15b-6HIS-SUMO-$btpeA^{R439A}$-AmpR	This paper	N/A
pET15b-6HIS-SUMO-$btpeA^{Y499A}$-AmpR	This paper	N/A
pET15b-6HIS-SUMO-$btpeA^{D500A}$-AmpR	This paper	N/A
pET15b-6HIS-SUMO-$btpeA^{D529A}$-AmpR	This paper	N/A
pET15b-6HIS-SUMO-Strep-$btpeA_{251\text{-end aa}}$-AmpR	This paper	N/A
pET15b-6HIS-SUMO-$btpiA_{19\text{-end aa}}$-AmpR	This paper	N/A
pET15b-6HIS-SUMO-$btpiA_{19\text{-end aa}}$-Strep-AmpR	This paper	N/A
pET15b-6HIS-SUMO-*btaeB*-AmpR	This paper	N/A
pET15b-6HIS-SUMO-$btaeB_{1\text{-}400\ aa}$-AmpR	This paper	N/A
pET15b-6HIS-SUMO-$btaeB_{1\text{-}410\ aa}$ -AmpR	This paper	N/A
pET15b-6HIS-SUMO-$colM_{31\text{-end aa}}$-AmpR	This paper	N/A
pET21b vector	Novagen	Cat# 69741-3
pET21b-*btpeA*-6HIS-AmpR	This paper	N/A
pET21b-*btaeB*-6HIS-AmpR	This paper	N/A
pET21b-$btaeB^{C460A}$-6HIS-AmpR	This paper	N/A
pET21b-$btaeB^{H546A}$-6HIS-AmpR	This paper	N/A
pET21b-*vgrG*-GSlinker-*btpeA*-6HIS-AmpR	This paper	N/A

(*Continued on next page*)

Continued

REAGENT or RESOURCE	SOURCE	IDENTIFIER
pET21b-*vgrG*-Drice-GSlinker-*btpeA*-6HIS-AmpR	This paper	N/A
pET22b vector	Novagen	Cat# 69744-3
pET22b-pelB-*btpeA*-6HIS-AmpR	This paper	N/A
pET22b-pelB-$btpeA_{1\text{-}120\ aa}$-6HIS-AmpR	This paper	N/A
pET22b-pelB-$btpeA_{121\text{-}250\ aa}$-6HIS-AmpR	This paper	N/A
pET22b-pelB-$btpeA_{251\text{-}end\ aa}$-6HIS-AmpR	This paper	N/A
pET22b-pelB-$btpeA^{H434A}$-AmpR	This paper	N/A
pET22b-pelB-$btpeA^{R439A}$-AmpR	This paper	N/A
pET22b-pelB-$btpeA^{Y499A}$-AmpR	This paper	N/A
pET22b-pelB-$btpeA^{D500A}$-AmpR	This paper	N/A
pET22b-pelB-$btpeA^{D529A}$-AmpR	This paper	N/A
pET22b-pelB-*colM*-AmpR	This paper	N/A
pET26b vector	Novagen	Cat# 69862-3
pET26b-pelB-$btpiA_{19\text{-}end\ aa}$-Strep-KanR	This paper	N/A
pET28a vector	Novagen	Cat# 69864-3
pET28a-6HIS-$btaeB_{8\text{-}end\ aa}$-KanR	This paper	N/A
pET28a-6HIS-$btaeB_{8\text{-}387\ aa}$-KanR	This paper	N/A
pET28a-6HIS-$btaeB_{8\text{-}387\ aa}^{K188A}$-KanR	This paper	N/A
pRSF-Duet vector	Novagen	Cat# 71341-3
pRSF-Duet-*btapC*-Strep-KanR	This paper	N/A
pRSF-Duet-Strep-*vgrG*-KanR	This paper	N/A
pNBU2-$P1T_{DP}^{GH023}$ –ermG	Lim et al.[57]	PMID_28431252
pNBU2-$P1T_{DP}^{GH023}$ –CmR	This paper	N/A
pNBU2-$P1T_{DP}^{GH023}$-*btaeB*-CmR	This paper	N/A
pNBU2-$P1T_{DP}^{GH023}$-ss-*btaeB*-CmR	This paper	N/A
pNBU2-$P1T_{DP}^{GH023}$-ss-$btaeB^{C460A}$-CmR	This paper	N/A
pNBU2-$P1T_{DP}^{GH023}$-ss-$btaeB^{H546A}$-CmR	This paper	N/A
pNBU2-$P1T_{DP}^{GH023}$-ss-*btaeB-btaiB*-CmR	This paper	N/A
pNBU2-P_{TonB3}-CmR	Tong et al.[58]	PMID_39389974
pNBU2-P_{TonB3}-$bfi1_{GS086}$-CmR	This paper	N/A
pNBU2-P_{TonB3}-*btpiA*-CmR	This paper	N/A
pNBU2-P_{TonB3}-*btaiB*-CmR	This paper	N/A
pNBU2-P_{TonB3}- -$btapC^{HA\text{-}HIS}$	This paper	N/A
pNBU2-P_{rhaR}-CmR	Jiang et al.[2]	PMID_38082149
pNBU2-P_{rhaR}-*btpeA*-CmR	This paper	N/A
pNBU2-P_{rhaR}-*btaeB*-CmR	This paper	N/A
pSIE1-$P1T_{DP}^{GH023}$-ss-*bfe1-bte1*-ErmR	Bencivenga-Barry et al.[59]	PMID_31712278
pSIE-$P1T_{DP}^{GH023}$-ss-*RS10745*-Δ*tssC*-CmR	This paper	N/A
pSIE-$P1T_{DP}^{GH023}$-ss-*RS10745*-Δ*btpeA*-CmR	This paper	N/A
pSIE-$P1T_{DP}^{GH023}$-ss-*RS10745*-Δ$btpeA_{1\text{-}155\ aa}$-CmR	This paper	N/A
pSIE-$P1T_{DP}^{GH023}$-ss-*RS10745*-Δ$btpeA_{156\text{-}end\ aa}$-CmR	This paper	N/A
pSIE-$P1T_{DP}^{GH023}$-ss-*RS10745*-KI-$BtpeA^{D529A}$-CmR	This paper	N/A
pSIE-$P1T_{DP}^{GH023}$-ss-*RS10745*-Δ*btaeB*-CmR	This paper	N/A

(*Continued on next page*)

Continued		
REAGENT or RESOURCE	SOURCE	IDENTIFIER
pSIE-P1T$_{DP}^{GH023}$-ss-*RS10745*-Δ*btaeB*$_{401\text{-end aa}}$-CmR	This paper	N/A
pSIE-P1T$_{DP}^{GH023}$-ss-*RS10745*-Δ*btaeB*$_{411\text{-end aa}}$-CmR	This paper	N/A
pSIE-P1T$_{DP}^{GH023}$-ss-*RS10745*-KI-BtaeB^{H546A}-CmR	This paper	N/A
pSIE-P1T$_{DP}^{GH023}$-ss-*RS10745*-Δ*btpiA*-CmR	This paper	N/A
pSIE-P1T$_{DP}^{GH023}$-ss-*RS10745*-Δ*btaiB*-CmR	This paper	N/A
pSIE-P1T$_{DP}^{GH023}$-ss-*RS10745*-Δ*btapC*-CmR	This paper	N/A
pSIE-P1T$_{DP}^{GH023}$-ss-*RS10745*-KI-Strep-*vgrG*-CmR	This paper	N/A
pSIE-P1T$_{DP}^{GH023}$-ss-*RS10745*-KI-HA-*btapC*-CmR	This paper	N/A
Software and algorithms		
AlphaFold2	AlphaFold Protein Structure Database	https://alphafold.ebi.ac.uk/
Coot 0.9.8.1	Emsley and Cowtan[60]	PMID_15572765
PyMOL 3.1	Schrödinger	N/A
InterPro	Blum et al.[41]	PMID_ 39565202
ChimeraX 1.4	Meng et al.[61]	PMID_ 37774136
cryoSPARC 4.4.1	Punjani et al.[62]	PMID_28165473
Phenix 1.21.1	Liebschner et al.[63]	PMID_ 31588918
JackHMMER	Potter et al.[40]	PMID_ 29905871
BLAST+, v.2.12.0+	Camacho et al.[64]	PMID_ 20003500
MAFFT, v.7.487	Katoh and Standley[65]	PMID_ 23329690
IQTREE (v.2.1.4_beta)	Minh et al.[66]	PMID_ 32011700
Clinker	Gilchrist and Chooi[67]	PMID_ 33459763
Dali server	Holm[42]	PMID_ 35610055
Prism v.9.3.0.	GraphPad	N/A
SignalP v5.0	Almagro Armenteros et al.[39]	PMID_ 30778233
Other		
Vitrobot Mark IV	Thermo Fisher Scientific	N/A
300 kV Titan Krios G4 microscope	Thermo Fisher Scientific	N/A
LSM900 laser scanning confocal microscope	Zeiss	N/A
LC-20AT HPLC	Shimadzu	N/A

EXPERIMENTAL MODEL AND SUBJECT DETAILS

Bacterial strains and growth conditions

All strains used in this study are listed in the key resources table. All *Bacteroides* strains were grown anaerobically at 37°C in brain heart infusion medium containing L-cysteine (1 g/L) and hemin (5 mg/L) (BHI) for liquid cultures, or on BHI agar plates (15% m/v agarose). *E. coli* strains were grown aerobically at 37°C in lysogeny broth (LB) medium for liquid cultures, or on LB agar plates (15% m/v agarose). Antibiotics (final concentrations: kanamycin 50 μg/mL, ampicillin 100 μg/mL, gentamicin 200 μg/mL and chloramphenicol 15 μg/mL) were added to the medium when required. Anhydrotetracycline (aTC) was dissolved in 100% ethanol at 200 μg/mL as stock solution and diluted 1000× when used for counter selection. Isopropyl β-D-1-thiogalactopyranoside (IPTG) was dissolved in sterilized ddH_2O and used at a final concentration of 0.2 mM.

Animal experiments

All animal experiments were supervised and approved by the Animal Research Ethical Inspection Form of Shandong University School of Life Sciences (SYDWLL-2024-001). Seven-week-old C57BL/6J specific-pathogen-free (SPF)-level female mice were purchased from GemPharmatech Co., Ltd. (Jiangsu, China). The mice were group housed in a controlled environment with strict adherence to SPF standards, including temperature maintained at 25 ± 2°C, humidity at 45 ± 5%, and a light-dark cycle of 12 hours each. They had unlimited access to autoclaved water and irradiated food. Prior to our studies described below, all mice underwent a one-week acclimatization period during which they remained healthy. The mice were treated with an antibiotic cocktail according to previously established protocols.[2] Specifically, antibiotic cocktails (10 mg of each of vancomycin, metronidazole, neomycin, and ampicillin per mice) were administered by oral gavage daily for 5 days. Subsequently, all antibiotic-treated mice were fed with autoclaved water supplemented with antibiotic cocktails (0.5 g/L vancomycin, 1.0 g/L metronidazole, 1.0 g/L neomycin, and 1.0 g/L ampicillin) and irradiated feed for 7 days. After 7 days, all antibiotic-treated mice were fed with autoclaved water and irradiated feed for 3 days. Then the fecal pellets were collected and tested for bacterial growth on BHIS agar supplemented with 200 μg/mL gentamycin and 15 ug/mL chloramphenicol. Only mice that showed no bacterial growth on either medium were included in the study. The antibiotic-treated mice were randomly divided into multiple groups (five mice per group). All antibiotic-treated mice received an equal mixture comprising 2.5×10^9 c.f.u of both prey strains and 2.5×10^9 c.f.u of killer strains via oral gavage. Fresh fecal samples were collected at the indicated time points for monitoring colonization. The collected samples were weighed, mashed, and vortexed in 1 mL PBS buffer before being diluted for counting c.f.u. The diluted fecal samples were then plated separately on selective BHI plates containing 200 μg/mL gentamycin and 15 μg/mL chloramphenicol.

METHOD DETAILS

Plasmid construction

All plasmids used in this study are listed in the key resources table. Wildtype constructs were generated through Gibson assembly,[68] while mutant constructs were generated using the quick-change method.[69] All plasmids were validated by Sanger Sequencing (Sangon BioTech). The maintenance and transformation of plasmid constructs followed standard molecular cloning procedures. The *Bacteroides*-derived periplasmic/cytoplasmic proteins were cloned into the backbone vector with or without an N-terminal signal peptide *pelB* for stable expression in the periplasm of *E. coli*. The plasmids were fused with N- or C-terminal tag for affinity purification as needed.

For aTC-induced expression in *Bacteroides*, the target genes were cloned into a pNBU2-P1T$_{DP}^{GH023}$ vector.[57,70] For constitutive expression in *Bacteroides*, the target genes were cloned into a pNBU2-Pro$_{tonB3}$ vector. For *in situ* genetic manipulation in *Bacteroides*, ~1 kb overlap upstream and downstream of the target region were cloned into Psie-P1T$_{DP}^{GH023}$-SS-RS10745 vector[59] containing M074_RS10745 (Protein ID: WP_025814153.1) as a counterselection marker.[36] The N-terminal signal peptide *ss* was used for stable expression in the periplasm of *Bacteroides* species.

Protein expression and purification

The protein expression and purification were conducted as previously described with minor modification.[71] Specifically, the *E. coli* BL21 (DE3) strains carrying plasmids for overexpression of recombinant proteins were cultured in LB medium supplemented with appropriate antibiotics at 37°C until reaching an optical density at 600 nm (OD_{600}) of 0.8, then induced overnight at 20°C by addition of 0.2 mM IPTG. Bacterial cells were harvested by centrifugation and lysed using a high-pressure cell disruptor (Union-Biotech) in lysis buffer (20 mM Tris 8.0, 150 mM NaCl) supplemented with 1 mM phenylmethylsulfonyl fluoride (PMSF) and 50 μg/mL DNase. The lysate was further centrifuged to eliminate cellular debris. The resulting supernatant was loaded onto either Ni-NTA agarose resin (Qiagen) or Strep-affinity resin (IBA Lifesciences), washed three times with 10 mL lysis buffer with (for Ni-NTA agarose resin) or without (for Strep-Tactin resin) 20 mM imidazole. The protein bound to the resin was then eluted by either Ni-NTA elution buffer (20 mM Tris 8.0, 150mM NaCl and 250mM imidazole) or Strep-Tactin elution buffer (100 mM Tris 8.0, 1 mM EDTA, 150 mM NaCl, 50 mM Biotin). The 6×HIS-SUMO tag was cleaved with ULP1 protease at room temperature for 3 h, followed by elution using lysis buffer. Subsequently, the sample was further purified through an anion-exchange column (Hitrap Q, GE Healthcare) and gel filtration chromatography (Superdex 200 Increase 10/300 GL, GE Healthcare).

Protein crystallization and structure determination

For the BtpeA$_{251\text{-end}}$-BtpiA$_{19\text{-end}}$ complex, the purified BtpeA$_{251\text{-end}}$ and BtpiA$_{19\text{-end}}$ were mixed with a molar ratio of 1:2 and incubated for 1 h at 4°C. The complex was further purified by gel filtration chromatography using an AKTA purifier System.

The crystals of BtpeA$_{251\text{-end}}$-BtpiA$_{19\text{-end}}$ complex (5mg/mL) and BtaeB$^{8\text{-}387}$ (7mg/mL) were grown at 18°C using the hanging-drop vapor diffusion method by mixing the protein and mother liquid at 1:1 ratio. The conditions for crystallization were as follows:

BtpeA$_{251\text{-end}}$-BtpiA$_{19\text{-end}}$ complex: 0.1 M Sodium Citrate (PH=5.0), 20% PEG 8000;

BtaeB$_{8\text{-}387}$: 0.1 M Sodium acetate (PH=5.2), 16% PEG3350.

Single-wavelength X-ray diffraction data were collected at 100K on BL02U1 and BL10U2 beamlines of the Shanghai Synchrotron Radiation Facility (SSRF). The diffraction data were auto-processed by Aquarium pipeline.[72] The phase determination was conducted through molecular replacement in Phenix[63] employing models generated by AlphaFold2.[73] Minor adjustments to the model were

manually performed using Coot[60] during iterative rounds of refinement with Phenix. The final data collection and refinement statistics are summarized in Table S1. All structure figures were generated using ChimeraX.[61]

Cryo-EM sample preparation and data collection

The purified VgrG protein was mixed with the purified BtpeA-BtaeB-BtapC ternary complex at a molar ratio of 1:2 and incubated on ice for 1 hour. Subsequently, the resulting VgrG-BtpeA-BtaeB-BtapC tetrameric complex was further purified using gel filtration chromatography.

Aliquots of 4 μL of purified VgrG-BtpeA-BtaeB-BtapC tetrameric complex at a concentration of approximately 0.35mg/mL was applied onto the glow-discharged cryo-EM grid (QUANTIFOIL Cu R1.2/1.3, 300 mesh) and then plunge-frozen into liquid ethane using a Vitrobot Mark IV (Thermo Fisher Scientific, Waltham, MA) (blotting force, 0; blotting time, 3s; wait time, 5s). 1,123 micrographs were collected using a 300 kV Titan Krios G4 microscope equipped with a K3 direct electron detector (nominal magnification, 105,000×; pixel size, 1.18Å; defocus range, -1.0 to -1.8 μm. The total electron dose for data collection was 60 $e^-/Å^2$.

Cryo-EM data processing

A total of 1,123 multi-frame movies were processed using cryoSPARC,[62] and a flowchart illustrating the process is provided in Figure S2. Motion correction with dose weighting was applied to image frames using patch motion correction, and patch contrast transfer function (CTF) estimation was performed on the motion-corrected micrographs. 169,280 particles were selected from 50 micrographs by Blob Picker, and subjected to 2D Classification. Subsequently, 56,107 particles were chosen as templates in the Template Picker to extract particles from 1,105 micrographs, resulting in a total of 646,324 particles extracted. Then, particles were subjected to 2D Classification, 333,307 particles were selected from Select 2D Classes after discarding bad particles. Three rounds of ab-initio reconstruction and heterogeneous refinement were employed to eliminate the remaining bad particles. Non-uniform refinement and local refinement were conducted using 106,021 particles. In the end, the map was obtained with resolution of 3.06 Å.

Model building into cryo-EM maps

The predicted models of VgrG, BtpeA and BtapC generated by AlphaFold2 were docked into the cryo-EM density map using Chimera and Phenix. However, due to the limited confidence in the predicted structure of BtaeB by AlphaFold2, it was hard to use it as a model to resolve the structure of BtaeB. To overcome this limitation, we determined the crystal structure of $BtaeB_{8-387}$ and successfully obtained an initial model for the VgrG-BtpeA-BtaeB-BtapC complex. Iterative model refinement was conducted through real-space refinement in Phenix, followed by adjustments in Coot. The detailed statistics of 3D reconstruction and model refinement are summarized in Table S2.

Conjugation and resistance selection

The plasmids were transformed into the donor strain *E. coli* S17- λ pir and conjugated into recipient *B. fragilis* strains, following previously described protocols with minor modifications.[58] Specifically, overnight cultures of *E. coli* S17- λ pir donor strains were diluted 200-fold in LB medium containing ampicillin, while *B. fragilis* recipients were diluted 100-fold in BHI medium. After approximately 3 h of growth, the donor (OD_{600} = 0.2-0.6) and recipient strains (OD_{600} = 0.1-0.2) were mixed at a volume ratio of 1:10 and centrifuged at 9,000*g* for 10 min. The pellet was resuspended in 100 μL of BHI medium and spotted onto a non-selective BHI plate for incubation under aerobic conditions at 37°C for approximately 20 hours to facilitate conjugation. Mating lawns were resuspended in 1 mL of BHI medium then different dilutions (1, 1/5, 1/10) of the resuspension (100 μL each) were plated onto selective BHI agar plates containing gentamycin and chloramphenicol. The single colonies were restreaked and verified by PCR after 2 to 3 days of anaerobic selection.

In situ genetic manipulation in *Bacteroides*

In situ genetic manipulation in *Bacteroides* is based on double-crossover allelic exchange using pSIE series plasmids (See key resources table). The verified single-crossover merodiploids (refer to "conjugation and resistance selection" above) were cultured overnight in 1 mL of BHI medium, and 100 μL of a 10^{-3}–10^{-4} dilution was plated onto a BHI plate containing 200 ng/mL aTC to isolate colonies that had successfully excised the counter selection marker. After incubating for 36 to 48 h, individual colonies were restreaked and verified by PCR. Sanger sequencing was performed to distinguish between wild type and mutant strains, as well as confirm the loss of the counter-selection marker.

The 1.0-kb homology regions corresponding to the upstream and downstream flanking regions of the knockout gene were cloned into the pSIE series plasmid to achieve the gene knockout. For gene knockin, three gene fragments were sequentially integrated into the pSIE series plasmids in the following order: 1.0-kb homology upstream of the gene insertion site, the inserted gene, and 1.0-kb homology downstream of the gene insertion site. *In situ* effector point mutants were generated by first knocking out the native effector and then inserting the mutated effector sequence.

Agar spot assay

To assess the inhibitory effect of BtpeA or BtaeB, we induced the expression of effector (including effector variants) and its immunity protein (including immunity protein variants) in the periplasm of the recipient strains. The pET-*pelB* series plasmids were used to

induce the expression of BtpeA in the periplasm of *E. coli* recipient strains, and the pNBU2-P1T$_{DP}^{GH023}$-*SS* series plasmids were used to induce the expression of BtaeB in the *B. fragilis* recipient strains. All inducible plasmids are listed in the key resources table.

The recipient strains carrying inducible plasmids were cultured referring to the protocol described in "bacterial strains and growth conditions". Briefly, the recipient strains were cultured to an exponential phase in 1 mL of medium at 37°C, and the density was adjusted to an OD_{600} of 0.5∼0.7. Following a 10-fold gradient dilution, 2.5 μL of each strain was spotted onto plates with or without the inducer. Plates without any inducer served as controls. The inducer IPTG was added at a final concentration of 0.2 mM, while the inducer aTC was used at a final concentration of 100 ng/mL. After overnight incubation at 37°C, the inhibitory effect was assessed. All recipient strains carrying inducible plasmids are listed in the key resources table.

Fluorescence microscopy

To examine the morphological characteristics of effector-treated strains, recipient strains carrying inducible plasmids were cultured overnight and subsequently diluted 100-fold in medium supplemented with an inducer (0.2 mM IPTG or 50 ng/mL aTC) for further culture for 6 h. Then, the collected culture was incubated with FM1-43 dye at a concentration of 5 μg/mL for an additional hour. The stained samples were visualized using a Zeiss LSM900 laser scanning confocal microscope.

Co-culture/competition assay *in vitro*

The prey strains were rendered chloramphenicol resistant (CmR) by transformation with the pNBU2-CmR plasmid, enabling screening on selective BHI plates. The killer and prey strains were cultured overnight in BHI medium, followed by a 1:100 dilution in 10 mL of fresh BHI medium and anaerobic cultivation for approximately 3.5 h until the optical density reached OD_{600} = 0.4. Subsequently, the killer and prey strains were mixed at a volume ratio of 10:1 and centrifuged at 9,000*g* for 10 min. The pellet was resuspended in 200 μL of BHI medium, and 20 μL of the resuspension was spotted onto a sterilized filter with a pore size of 0.22 μm placed on a non-selective BHI plate for co-culture under anaerobic conditions at 37°C for approximately 24 hours. Mating lawns were resuspended in 1 mL of BHI medium, followed by a 10-fold gradient dilution; subsequently, each co-culture resuspension (2.5 μL) was spotted onto selective BHI plates containing chloramphenicol to assess the inhibitory effect or plated directly onto selective BHI plates containing chloramphenicol to quantify colony-forming units (c.f.u) of the prey strains.

Western immunoblot analysis

The strains to be tested were cultured anaerobically overnight in fresh BHI medium, followed by 1:100 dilution in 10 mL of fresh BHI medium and anaerobic cultivation for approximately 4.5 h until the optical density reached OD_{600} = 0.6. Subsequently, the 5 mL of collected culture was centrifuged at 9,000*g* for 10 min. The pellet was then resuspended in 200 μL of PBS buffer (3.2 mM Na_2HPO_4, 0.5 mM KH_2PO_4, 1.3 mM KCl, 135 mM NaCl, pH 7.4). Meanwhile, the supernatant was filtered through a 0.22 μm filter and concentrated to ∼200 μL by ultrafiltration (10 kDa cutoff, Millipore). The resuspension and concentrated supernatant were boiled in 200 μL of 2× SDS loading buffer (100 mM Tris 6.8, 200 mM DTT, 4% w/v SDS, 0.1% w/v Bromothymol blue, 20% Glycerol) to respectively prepare whole cell lysate (WCL) and supernatant (SUP) samples.

For Western immunoblot analysis, the samples were electrophoresed on 15% Glycine-SDS-PAGE gels. The gel contents were subsequently transferred onto polyvinylidene difluoride membranes (Millipore), blocked, and probed with primary antibodies (Rabbit α-BtpeA, α-BtaeB and α-Hcp1, this study, used at a dilution of 1:3000; Rabbit α-DnaK, Cusabio #CSB-PA633459HA01EGW, used at a dilution of 1:3000; Mouse α-strep, MBL #M211-3, used at a dilution of 1:2000 dilution; Mouse α-HA, MBL #M180-3, used at a dilution of 1:2000). Subsequently, horseradish peroxidase-conjugated secondary antibodies (goat anti-rabbit, MBL #458, diluted to 1:5000; goat anti-mouse, MBL #330, diluted to 1:5000). All protein bands were visualized using the M5 HiPer ECL Western HRP Substrate (Mei5 Biotechnology, MF074-05) and captured using the Tanon-5200 Chemiluminescent Imaging System (Tanon).

Co-immunoprecipitation and immunoblotting analysis

To assess the *in vivo* formation of the quaternary complex (VgrG-BtpeA-BtapC-BtaeB) or other indicated complex, *B. fragilis* GS086-Strep-VgrG-BtapC-HA and its isogenic mutants were cultured anaerobically overnight in fresh BHI medium. The culture was then diluted 1:100 in 1 L of fresh BHI medium and further anaerobically cultivated for approximately 5 h until reaching an optical density of OD_{600} ∼0.8. The collected culture was resuspended in 25 mL of lysis buffer and lysed using a high-pressure cell crusher (Union-Biotech). The supernatant from the lysate was collected and subjected to at least three rounds of loading onto HA-affinity resin (50 μL), followed by washing with lysis buffer at least three times (10 mL each time). Subsequently, 50 μL of proteins-bound HA-affinity resins were collected and boiled with 50 μL of 2× SDS loading buffer to prepare output samples. The supernatant from lysate without HA-affinity chromatography served as input samples. Both input and output samples were loaded at a volume of 10 μL each for subsequent western blot analysis according to the protocol described above "western immunoblot analysis". Western immunoblot analysis was performed when necessary.

Pull-down assay

The purified bait protein and prey protein were combined in a 2:1 ratio to assess the formation of complex *in vitro*. After incubation at 4°C for 1 h, 50 μL of Ni-NTA resin (Qiagen) or Strep-Tactin resin (IBA Lifesciences) was added, and incubated for an additional hour. To enrich the target protein in the supernatant of *B. fragilis* GS086 and its isogenic mutant, 30 μL of Ni-NTA resin was directly added to the 2 mL of 50× concentrated supernatant and then incubated at 4 °C for more than two hours. The resins were washed three times

with lysis buffer containing 0.05% Triton X-100. Protein bonded to the resin was eluted using either Ni-NTA elution buffer or Strep-Tactin elution buffer. Samples were separated and evaluated by electrophoresis using 15% Glycine-SDS-PAGE gels.

Phosphatase activity assay

The Phosphatase activities of BtpeA were assessed following the manufacturer's protocols (Biosharp, BL709A). Briefly, 20 μg purified BtpeA or its mutants in 10 μL lysis buffer were added to 100 μL of BCIP (5-bromo-4-chloro-3-indolyl-phosphate)/NBT (nitro blue tetrazolium) premixed solution. The premixed BCIP/NBT solution was employed as the substrate pair, and the enzymatic product NBT-formazan was quantified by measuring OD_{600}. An equal volume of enzyme buffer (lysis buffer) was used as a control instead of BtpeA. After incubating aerobically at 37°C for 3 h, the absorbance at 600 nm was measured using a Tecan Infined 200 Pro spectrophotometer (Tecan).

Extraction of lipids from membrane fractions

The membrane lipids were extracted as described above with minor modifications.[74,75] For *in vivo* detection of lipid II phosphatase activity of BtpeA or ColM, *E. coli* BL21 carrying indicated inducible periplasmic (ColM, BtpeA, BtpeA mutants and BtpeA-BtpiA complex) expression plasmids, cultured in 1L LB supplemented with appropriate antibiotics at 37°C, 200 rpm until OD_{600} reached 0.1-0.2. Subsequently, IPTG was added to a final concentration of 0.2 mM and induced at 37°C and 200 rpm for approximately 5 hours before harvesting. Cells were harvested from 1L LB cultures through centrifugation, and the resulting pellets were resuspended in PBS buffer. High-pressure cell crusher (Union-Biotech) was employed for lysing the cells, followed by centrifugation at 20,000*g* for 20 min to eliminate cellular debris. After ultra-centrifugation at 150,000*g* for 60 min, the membrane pellet was resuspended in 0.5 mL PBS buffer (Taking 1 L periplasmic expression of toxic protein BtpeA or ColM as an example, when expressing non-toxic protein, the amount of resuspending PBS buffer should be expanded according to the actual amount of harvested cultures). Then, methanol (1.25 mL) and chloroform (625 μL) were added. The suspension was vortexed for 2 min at room temperature, and the homogenates were centrifuged at 7,100*g* for 10 min at 4°C. Chloroform (625 μL) and PBS (625 μL) were added to the supernatants, and they were vortexed and centrifuged at 7,100*g* for 10 min at 4°C to separate the chloroform phase from the PBS–methanol phase. The isolated chloroform phase was then vacuum dried. Dried pellets containing the purified membrane lipids were resuspended in 100 μL of the HPLC mobile phase solvents (20% isopropanol with 0.1 % formic acid + 80% methanol with 0.1 % formic acid).

HPLC analysis of membrane lipids

The 20 μL of lipids extracts resuspended in HPLC mobile phase solvents were analyzed using isocratic HPLC (Shimadzu LC-20AT HPLC) equipped with a reversed-phase octadecyl silica (ODS) C18 column (5 μm particle size, 100 Å pore size, 50 × 2.1 mm). A flow rate of 0.5 mL/min was maintained, and the column temperature was set at 55°C. Detection of enzymatic products performed at a wavelength of 210 nm.

Preparation of peptidoglycan

The insoluble peptidoglycan was prepared from *E. coli* MG1655 as previously described with minor modification.[76] Specifically, *E. coli* MG1655[77] strains were cultured overnight in fresh LB medium, followed by 1:100 dilution in 1 L of fresh LB medium for further cultivation until the optical density reached OD_{600} ~0.7, which took approximately 4.5 h. The collected culture was resuspended in 10 mL of PB buffer (25 mM phosphate buffer, pH 6) and gradually mixed drop by drop with an equal volume of boiling SDS-PB buffer (8% W/V) under vigorous stirring. The mixture was boiled for 2-3 h until it became homogeneous. Sacculi were repeatedly washed with ddH_2O through ultracentrifugation (130,000*g*, 30 min, 20°C) until SDS was completely removed. Then, overnight trypsin digestion (100 μg/mL) was performed to remove other peptidoglycan-associated proteins. Overnight trypsin-treated samples were mixed drop by drop with an equal volume of boiling SDS-PB buffer (8% W/V). Repeat the previous ddH_2O-washed procedures until total removal of SDS. Finally, the peptidoglycan was resuspended in 1 mL of PB buffer (1 mL of PB buffer for 1 L *E. coli* MG1655 culture) and stored at -20°C. For each reaction, it is recommended to use a 40 μL aliquot of purified peptidoglycan.

Digestion of Peptidoglycan and HPLC analysis

The digestion of peptidoglycan and HPLC analysis was performed as previously described with minor modifications.[76] Specifically, 40 μL of purified peptidoglycan were incubated with 20 μg purified BtaeB or its variants in 10 μL of lysis buffer for 5 h to overnight at 37°C. An equal volume of enzyme buffer (lysis buffer) instead of BtaeB served as a control. Overnight BtaeB-treated samples were then incubated with 10 μL of 1 mg/mL mutanolysin solution for 4 h at 37°C. The mutanolysin-treated samples were transferred to the pre-equilibrated Amicon Ultra-0.5 Centrifugal Filter (10 kDa cutoff, Millipore) and centrifuged at 14,000*g* for 20 min to collect soluble peptidoglycan fragments. These fragments were subsequently reduced by adding an equal volume of sodium borohydride solution (final concentration 10 mg/mL, dissolved in 250 mM borate buffer) for 30 min. Finally, the pH value of each reaction was adjusted to 2-4 by adding approximately 3 μL of 85% phosphoric acid before preparing samples for HPLC analysis.

The 20 μL of reduced soluble peptidoglycan fragments were analyzed using HPLC (Shimadzu LC-20AT HPLC) equipped with a reversed-phase octadecyl silica (ODS) C18 column (5 μm particle size, 100 Å pore size, 50 × 2.1 mm). Separation of the soluble peptidoglycan fragments was achieved by employing a gradient elution method. Solvent A consisted of HPLC-grade water containing 0.1% formic acid, while solvent B comprised 50% acetonitrile and 50% HPLC-grade water with 0.1 % formic acid. The separation process was carried out at a flow rate of 0.6 mL/min over a linear gradient lasting for 120 minutes at a column temperature of 30°C,

and detection was performed at a wavelength of 206 nm. Identification of individual peaks was assigned by comparison of their retention times and profiles to validated chromatograms.[48] Quantification of each type of peptidoglycan fragment can be determined by measuring the area under the peak using the software provided with HPLC system.

Analysis of GS086-like type T6SS V2 region

The BtapC protein exhibits a high degree of conservation in all GS086-like type T6SS V2 regions. Therefore, a tblastn (BLAST+, v.2.12.0+) query (e-value $\leq$ 1e−10)[64] was performed using BtapC against an in-house nucleotide database consisting of whole genome sequences of *B. fragilis* from NCBI Genome datasets (Update to December 2024, 1623 whole genome sequences) to identify the GS086-like type T6SS V2 region. The three proteins within the V2 region of GS086-like type T6SS were fused in the order of BtpeA, BtapC, and BtaeB.

The representative fused protein sequences were aligned using MAFFT (v.7.487)[65] while retaining the alignment blocks. Maximum-likelihood phylogenetic trees were constructed using IQTREE (v.2.1.4_beta)[66] after automatic model selection, with nodal support assessed through 1000 ultrafast phylogenetic bootstraps.

Analysis of single or two effectors-containing T6SS V2 region

The tblastn (BLAST+, v.2.12.0+) query (e-value $\leq$ 1e−10) was performed using PAAR (BF9343_RS09410) against an in-house nucleotide database consisting of whole genome sequences of *B. fragilis* from NCBI Genome datasets (Update to December 2024, 1623 whole genome sequences) to identify the single effector-containing T6SS V2 region. The tblastn query was performed using BtapC or BtapC homologues (H4 or h4) against in-house nucleotide database to identify two effectors-containing T6SS V2 region.

Analysis of BtapC-homologues in Bacteroidota Species

The BtapC protein in GS086 was used as a query (e-value $\leq$ 1e−10) in a tblastn (Algorithm: PSI-Blast) (BLAST+, Version 2.12.0+) search against the NCBI Nr/Nt database, with *B. fragilis* excluded. The BtapC homologues-containing loci were aligned and visualized using Clinker.[67]

Structural similarity search

The Dali server[42] was utilized with default settings to search for structural homologues of BtpeA and BtaeB.

QUANTIFICATION AND STATISTICAL ANALYSIS

Data are presented as the arithmetic mean ± standard deviation (SD) unless otherwise indicated. All statistical analysis were calculated using GraphPad Prism v.9.3.0., Unpaired two-tailed Student's *t*-tests were used for comparing means between two groups, unless otherwise indicated. The significance of mean comparisons was denotated as follows: NS, not significant; **P*< 0.05; ***P*< 0.01; ****P*< 0.001; *****P*< 0.0001. A significance level of *P*< 0.05 was considered statistically significant. No specific statistical methods were used to pre-determine sample sizes but our sample sizes are comparable to those reported in previous publications. When applicable, samples and animals were randomly assigned to different groups. Data collection and analysis were not conducted in a blinded manner with respect to experimental conditions. No data points were excluded.